EXPLORING LINEAR RAKE MACHINING IN 316L AUSTENITIC STAINLESS STEEL FOR MICROSTRUCTURE SCALE-REFINEMENT, GRAIN BOUNDARY ENGINEERING, AND SURFACE MODIFICATION

by

Giovanni Giuseppe Facco

B.S., Nuclear Engineering, Pennsylvania State University, 2005

M.S., Materials Science and Engineering, University of Pittsburgh, 2009

Submitted to the Graduate Faculty of

the Swanson School of Engineering in partial fulfillment

of the requirements for the degree of

Doctor of Philosophy in Materials Science and Engineering

University of Pittsburgh

2013

UNIVERSITY OF PITTSBURGH

SWANSON SCHOOL OF ENGINEERING

This dissertation was presented

by

Giovanni Giuseppe Facco

It was defended on

July 3, 2013

and approved by

Ian Nettleship, Ph.D., Associate Professor, Department of Mechanical Engineering and Materials Science

Brian Gleeson, Ph.D., Professor, Department of Mechanical Engineering and Materials Science

Anthony J. DeArdo, Ph.D., Professor, Department of Mechanical Engineering and Materials Science

M. Ravi Shankar, Ph.D., Associate Professor, Department of Industrial Engineering

Dissertation Director: Jörg M.K. Wiezorek, Ph.D., Associate Professor, Department of Mechanical Engineering and Materials Science

EXPLORING LINEAR RAKE MACHINING IN 316L AUSTENITIC STAINLESS STEEL FOR MICROSTRUCTURE SCALE-REFINEMENT, GRAIN BOUNDARY ENGINEERING, AND SURFACE MODIFICATION

Giovanni Giuseppe Facco, Ph.D

University of Pittsburgh, 2013

Thermo-mechanical processing plays an important role in materials property optimization through microstructure modification, required by demanding modern materials applications. Extreme grain size refinement, grain boundary engineering, and surface modification have been explored to establish enhanced performance properties for numerous metals and alloys in order to meet challenges associated with improving degradation resistance and increasing lifetime in harsh environments. Due to the critical role of austenitic stainless steels, such as 316L, as structural components in harsh environments, e.g. in nuclear power plants, improved degradation resistance is desirable. Linear raking, a novel two dimensional plane strain machining process, has shown promise achieving significant grain size refinement through severe plastic deformation (SPD) and imparting large strains in the surface and near surface regions of the substrate in various metals and alloys, imparting enhanced properties. Here, the effects of linear rake machining on the microstructure and related properties of 316L are investigated systematically for the first time. The controlled variation of linear raking processing parameters in combination with detailed micro-characterization using analytical electron microscopy, x-ray diffraction and associated property measurements enables the determination of the influence of changes in strain and strain rate on the developing deformation microstructure and related properties. Varying the linear raking process parameters, and consequently the strain and strain rate, affects the volume fractions of deformation induced α'-martensite and the degree of grain

refinement, to the nanoscale, through SPD in the chips produced. Additionally, linear raking is identified as a way to produce surface modified structures in the specimen substrate surface of 316L, with observations of various degrees of deformation and strain up to a depth of 150μm. This research clearly demonstrates that materials property modification can be achieved effectively by linear raking processing, and that resulting surface modified structures provide significant stored energy for recovery and recrystallization. This study provides a fundamental understanding of linear raking as a thermo-mechanical processing technique, which may in the future be capable of creating grain boundary engineered surface modified components for use in harsh environments like those in commercial nuclear power plants.

TABLE OF CONTENTS

LIST OF TABLES

LIST OF FIGURES

PREFACE

I would like to express my gratitude to all those who made this dissertation possible.

First, I would like to thank my dissertation advisor Dr. Jörg Wiezorek, whose guidance and insight has proved invaluable throughout doctoral studies. I would also like to thank my committee members Professors Brian Gleeson, Anthony DeArdo, Ian Nettleship, and Ravi Shankar for their service, as well as sharing their knowledge and experience.

I would also like to express a deep gratitude towards Drs. Andreas Kulovits and Xiahan Sang, as well as my lab mates Kai Zweiacker and Yaakov Idell whose help and support have been immensely useful during my studies.

This work was funded by The Nuclear Regulatory Commission (NRC-38-09-935), and the National Science Foundation (NSF CMMI #0856626), and completed with the infrastructure support of the Materials Micro-Characterization as well as the Nano-Fabrication and Nano-Characterization laboratories in the Swanson School of Engineering at the University of Pittsburgh.

Finally, I would like to thank all those close to me who supported me during my time at the University of Pittsburgh, including my parents, Giuseppe and Lucia Facco; my sisters; Anna and Francesca; and Eleanor Gillette, who through their love, support, and nagging have pushed me farther than I ever could have on my own.

ABBREVIATIONS

NSF – National Science Foundation

NRC – Nuclear Regulatory Commission

NPP – Nuclear Power Plants

PWR – Pressurized Water Reactors

GB – Grain Boundary

GBC – Grain Boundary Character

GBCD – Grain Boundary Character Distribution

GBE – Grain Boundary Engineering

SCC – Stress Corrosion Cracking

IASCC – Irradiation Assisted Stress Corrosion Cracking

DPA – Displacements per Atom

RIS – Radiation Induced Segregation

SIM – Strain Induced Martensite

SPD – Severe Plastic Deformation

UFG – Ultrafine Grain

ECAP – Equal Channel Angular Processing

HPT – High Pressure Torsion

SMAT – Severe Mechanical Attrition Treatment

LSP – Laser Shock Peening

LPB – Low Plasticity Burnishing

1.0 INTRODUCTION

With a globally increasing demand for energy (electrical power), and due to economic and environmental pressures, domestic energy strategies strongly recommends reducing reliance on foreign and fossil fuels to meet domestic energy needs and to sustain national and global prosperity[1]. Proposed plans envisage expanded utilization of alternative, greenhouse gas emission free, renewable energy sources, and in parallel, using nuclear power plants (NPP) to support the electrical power base load for the next 20-50 years, while the technologies for advanced renewable energy sources are developed [1, 2]. This strategy requires the continued operation of existing NPP beyond their original 40-year operating license life-time as well as the construction of new advanced NPP. The initial stage of extensions to a 60-year operating life has been completed for the majority of the domestic NPP [2, 3]. The operating life-time of commercial NPP and the service intervals of critical components are dictated by the degradation of structural materials used in the reactor vessel and as reactor internal components (i.e., not the fuel) [2-4]. The structural materials used in commercial NPP internal reactor core environments include Ni and Zr alloys, and stainless steels[4, 5]. In the NPP, these reactor internal materials are exposed to extreme environmental conditions of pressure (15 MPa or 150 atm), temperature (~620K ≈ 350 ˚C), mildly corrosive water based coolant mediums, and neutron irradiation[4, 6]. Note that irradiation can also affect an additional increase (of 50 – 100 K) in the temperature of large cross section components[6].

Due to the complex design concerns with regards to containment, safety, and performance, the introduction of new materials and alloys in NPP is very difficult. Therefore, microstructural engineering is the most economical way of achieving the improvements needed in order to modify already approved materials in such a way that their performance can meet the newly desired criteria for sustained extended safe operating life of NPP.

Austenitic stainless steels (i.e. 316L, 304L), which have a significant history of performance, behavior, testing and use, have long been an important part of the materials selection in NPP design due to their excellent corrosion resistance and thermo-mechanical properties. Additionally, outside the NPP reactor environments alloys like 316L are used as structural materials in biomedical, pharmaceutical, and petrochemical related applications, largely due to their excellent corrosion resistance. While these alloys are used in many of today's most advanced industries and subjected to some of the most extreme environments, both overall strength and long term failure mechanisms limit their potential use, particularly for extended exposure in the conditions within the reactors of NPPs [4].

Current processing techniques are broadly concerned with performance enhancement to gain improvement in high temperature properties, resistance to environmental degradation, and thereby facilitation of longer component lifetimes. To achieve performance enhancement in these areas, particular attention has been placed on grain size and grain size distribution, grain boundary (GB) character and GB character distribution, stored strain, residual stresses (tensile vs. compressive), chemistry (solute species and precipitate distribution), and micro-constituent phase fractions [7-9]. The application of these advanced processing techniques, which can affect microstructural changes needed to improve the performance of the materials already approved

for use in NPP, is of importance in efforts to accomplish the goals of achieving independent, and sustainable domestic energy production in the future.

In the case of the austenitic alloys used in nuclear reactors, considerable focus has been placed on properties that enhance resistance to surface initiated failures (i.e., fatigue strength, crack initiation, corrosion resistance, and susceptibility to the complex phenomena of stress corrosion cracking, SCC, and irradiation assisted SCC, IASCC) [4, 10-12]. In particular, surface modification techniques imparting mechanical property and microstructural changes to local regions near the surface of the component materials have been an area of interest to the nuclear industry. These sorts of processing paths would potentially allow for significantly increased lifetimes of components without the need to introduce completely new materials or new component designs, which can greatly assist in limiting the amount of effort and time required to secure licensing approval for domestic use in the highly regulated industry of civilian NPP.

In this work, as part of developing new and interesting processing techniques, a room-temperature two-dimensional plane-strain machining technique, known also as linear raking, is applied to 316L. This somewhat novel thermomechanical processing method has shown promise in other metals and metallic alloy systems, such as Ni, Al and Ti based alloys, facilitating through combination of very high strain rates and large strains that result in dramatically scale refined and stable microstructures in the chips produced during this process [13, 14]. Furthermore, preliminary evidence for severely deformed surface structures has been reported for linear raking processed, which indicates potential for the development of linear raking as a surface modification technique [14]. Here a first and detailed investigation of linear raking on the evolution of the microstructure and properties of 316L austenitic stainless steels has been performed, and the feasibility of utilizing the raking process as part of a processing path towards

preparation surface modifications designed to achieve enhanced performance regarding surface initiated failures is considered.

1.1 FUTURE IMPACT

The development of linear raking as a new, effective processing route which could mitigate long-term failures would be beneficial to the prolonged operations of materials in environments where replacement and retrofitting of components is difficult. Furthermore, fundamental processing advancements, improving overall behavior and properties, would also allow for a larger operational space in which these materials can be utilized, opening opportunities and increasing their effectiveness in more applications moving forward. Finally, by being able to extend the lifetime of commercial NPP both now and in the future provides a path towards their continued use as an important part of the national energy portfolio.

2.0 BACKGROUND

With the complex design challenges associated with commercial NPP technology, material selection is of utmost importance. High temperature, high strength, corrosion resistant materials, such as austenitic stainless steels, are thought to be an excellent choice regarding performance and durability for reactor internal support structures in the harsh environments of these reactors. However, as commercial NPPs continue to operate some of these stainless steel components are beginning to reach the end of their predicted safe-life. Understanding and predicting the end-of-life failure of these alloys has become an important issue, where materials originally not considered susceptible to certain degradation mechanism, such as irradiation assisted stress corrosion cracking (IASCC), are observed to suffer failures after extended in–service exposure [12]. For example 316L, an alloy used in baffle plate bolts, was not initially considered susceptible to SCC. However, in pressurized water reactor (PWR) NPP 316L-bolts have begun failing due to IASCC [12]. The failure of these materials due to irradiation related effects, which had been unexpected when the reactors were initially designed, has been investigated in detail [11, 15-17]. These failures indicate potential risk of unexpected failures in other structural components of the reactor internal systems and are therefore one of the primary obstacles to operating license extension for current NPP. An understanding how these failures and related failure mechanism(s) can be prevented and/or mitigated is important in developing new material processing paths to support improved resistance to irradiation assisted degradation of stainless

steels in NPP reactor internal environments. Additionally, modification of the currently quantified and certified stainless steels, currently in use for these applications, is preferred to replacing these components with parts made from new materials. This preference is due to the significant constraints associated with the certification process for entirely new materials, and the considerable experience and knowledge base within both the industrial and scientific sector regarding the behavior of austenitic stainless steels.

2.1 THE ROLE OF GRAIN SCALE REDUCTION AND GRAIN BOUNDARIES ON MITIGATING RADIATION RELATED FAILURE

It has long been understood that the reduction in grain size of polycrystalline aggregates has great advantages in terms of strengthening of metals and alloys [18]. Through grain size strengthening, generally described by the empirically established Hall-Petch relationship, great improvements in yield stress can be achieved for grain size refinements well into the nanocrystalline regime[19]. The role of grain size in mitigating SCC has been modeled and it has been shown that crack propagation rates might be reduced by decreasing the grain size [20]. This reduction in crack propagation is due to a crack tip shielding effect, where the overall increase in grain boundary density allows for a higher density per unit crack length of crack branches and bridges to be formed [20, 21]. These branches and bridges are able to slow crack growth by redistributing the internal stresses at the crack tip over larger volumes [20, 21]. Also the role of grain size, and relatedly grain boundaries, in mitigating irradiation defects and therefore irradiation related failures has been investigated [22, 23]. An important observation of the effects of irradiation on bulk microcrystalline austenitic stainless steels is the accumulation of

point defect clusters. These defects, like interstitial Frank loops, are known to form in increasing numbers in grain interiors in the early stages of NPP related neutron irradiation exposure, and are known to cause embrittlement detrimental to performance [17]. Frank loop populations act as obstacles to dislocation glide in the austenitic stainless steel grains, resulting in hardening, an increase in yield strength, and associated reduction in elongation to failure, and reduced toughness. Furthermore, the Frank loops, faulted loops with dislocations with Burgers vectors of type 1/3<111> bounding stacking faults on the {111} planes of the austenitic matrix with face centered cubic structure, also interact with interstitial species, such as carbon atoms, and substitutional solute atom species, such as Cr, Ni and Si, leading to segregation [17, 24]. Segregation and formation of precipitates, e.g. carbides, Si bearing intermetallics, is enhanced by effects from neutron irradiation, known as radiation induced segregation (RIS) [17]. By comparing the microstructures of UFG grain refined stainless steel to conventional micro-crystalline grain scale bulk solution annealed austenitic stainless steels, it has been shown that the nature of the grain refined material, in particular due to the higher grain boundary density, prevented the formation of Frank loops and the associated RIS at the Frank loop boundaries, which were observed in the micro-crystalline material, by allowing for point defect annihilation at the grain boundaries [24]. Since RIS of this nature is generally considered one of the major contributing factors in the development of susceptibility for IASCC, these later investigations show evidence of the promise of nanocrystalline scale grain refined materials for mitigating IASCC.

Additionally, for structural alloys based on face-centered cubic (FCC) matrices, such as austenitic stainless steels, it has been shown that controlling the character and distribution of grain boundaries, through grain boundary engineering (GBE), is of great importance in

improving the performance of these materials[25]. In particular, the presence of low energy grain boundaries (GB) has been shown to decrease susceptibility to sensitization to failure by stress-corrosion-cracking (SCC) [25-27]. Low energy GB include coherent twin boundary segments, as well as coincident-site boundaries (CSL) with large numbers of coincident sites (denoted as Σn , where n is the reciprocal of the density of coincident sites in the boundary plane, e.g. Σ3 and Σ9 correspond to grain boundaries where 1 in 3 and 1 in 9 lattice points coincide respectively). It has been suggested that these low energy GB provide improved resistance to SCC by limiting the intergranular precipitation of carbides in austenitic stainless steels [10, 25, 28, 29]. Intergranular Cr-rich carbide precipitation, which can occur in these alloys, depletes Cr levels in matrix grains in the vicinity of the Cr-rich GB precipitates and also at the grain boundary segments adjacent to the Cr-rich GB precipitate [5, 10, 28]. This local reduction in Cr content, which can prevent the formation of the adherent and protective chromium oxide scales that are the basis of corrosion resistance in austenitic stainless steels, results in deleterious effects regarding corrosion resistance [30]. The realization of significant property improvements by controlled changes in the GB character distribution (GBCD) has led to the widespread development of thermomechanical processing treatments termed grain boundary engineering (GBE) methods with the goal to obtain materials with high densities of low surface energy grain boundaries, i.e., low-Σn boundaries[7, 31]. GBE has been successfully developed for FCC based metals and alloys with intermediate to low stacking fault energies, which includes austenitic stainless steels [7, 31].

2.2 STRENGTHENING OF AUSTENITIC STAINLESS STEELS

Austenitic stainless steels are essentially single phase alloys, although very small volume fractions of retained delta ferrite or carbide precipitation may be present in commercial products, have excellent corrosion resistance combined with at least for steels a relatively low mechanical strength. Since they are used as a structural material and many degradation mechanisms, e.g. fatigue, creep, are improved by increased mechanical strength, it would be desirable to enhance their mechanical strength (e.g. yield stress, ultimate tensile strength, hardness). The requirements to maintain the excellent corrosion resistance and stability of the essentially single phase microstructures limits the approaches to strengthening of austenitic stainless steels, for instance precluding significant exploitation of precipitation strengthening. Hence, improving the mechanical strength of austenitic stainless steel typically includes conventional mechanical processing through cold working induced strain hardening and formation of strain-induced martensite (SIM) [32, 33]. Plastic deformation of these austenitic stainless steels at room temperature and below can locally produce the strain induced transformation of volumes of the FCC austenite matrix to the martensite, SIM. In 300 series austenitic stainless steels, SIM is generally formed at a given temperature after a critical strain and includes two types of crystallographically distinct forms of SIM, namely the hexagonal ε-martensite and the BCC α'-martensite [34-40]. Generally this transformation consists of a transformation sequence that can be considered somewhat continuous, increasing the amount of SIM formed from the austenitic γ-phase [35, 37, 39]. As the plastic strain increases initially γ-phase transforms locally to ε-phase and then to α'–phase as strain continues to increase [38, 39]. These strain induced transformations begin to occur at the onset of deformation where stacking faults associated with

glide activity of Shockley type partial dislocations accumulate and begin to interact to produce bands and where ε-martensite phase volumes nucleate[35, 38, 39]. With increasing plastic straining stacking faulted bands on multiple different glide planes in the austenite grains intersect, where multiple orientation variants of ε-phase have formed and locally begin to interact with each other, leading to formation of α'-phase martensite [35]. However, depending on the strain, strain rates and deformation temperature the sequential steps in the SIM formation may not be necessary and α'-phase martensite may form more directly from the strain destabilized austenite, γ→α', through direct dislocation interactions [37, 38]. The stacking fault energy (SFE) of a given austenitic stainless steel alloy is a major factor in determining its potential to form SIM in response to plastic deformation and therefore the amount of SIM present in the microstructures after plastic deformation processing [41] . Relationships between the SFE and the elemental composition have been developed empirically for austenitic stainless steels, e.g.:

$$\text{SFE } (mJ \cdot m^{-2}) = -53 - 0.7(\%Cr) - 6.2(\%Ni) - 3.2(\%Mn) - 9.3(\%Mo) \quad \textbf{(1)}$$

In a similar fashion as equation 1, empirical relationships have been established for the start temperature of the SIM formation, the martensite start temperature (M_s), e.g.[42]:

$$M_s\ (°C) = 1302 - 42(\%Cr) - 61(\%Ni) - 33(\%Mn) - 28(\%Si) - 1667(\%[C+N]) \quad \textbf{(2)}$$

Since the SIM formation is related to the amount of strain and the temperature at which the straining is performed, a useful composition dependent parameter is the temperature at which a fixed amount of plastic strain, e.g. that associated with a 30% tensile deformation, induces a

fixed amount of SIM volume fraction, e.g. 50% of transformation to SIM[36, 43]. This temperature or thermomechanical processing parameter, referred to as $M_{d(30/50)}$, can also be used to compare the composition dependent tendency or level of instability of the austenitic stainless steel regarding SIM transformation. The $M_{d(30/50)}$ parameters can be determined by the empirically obtained equation below [36]:

$$M_d\,(30/50) = 413 - 13.7(\%Cr) - 9.5(\%Ni) - 8.1(\%Mn) - 18.5(\%Mo) - 9.2(\%Si) - 462(\%[C+N]) \quad \textbf{(3)}$$

Table 1 collates the values of SFE, M_s and $M_d(30/50)$ for the 304L and 316L grade steels commonly used in NPP reactor internal components. Clearly, the 316L grade is more resistant to SIM formation than the 304L grade austenitic stainless steel, with higher SFE and a lower martensite start temperature.

Table 1 Nominal SFE, M_s and $M_d(30/50)$ values for 304L and 316L

Alloy	M_s (°C)	$M_{d(30/50)}$ (°C)	SFE ($mJ \cdot m^{-2}$)
316L	-448	-33.0	63.0
304L	-410	-44.0	28.7

The main drawbacks of forming SIM, which occurs even in the more stable 316L after plastic deformation processing, are reduced ductility and corrosion resistance[38]. Furthermore, both of these changes (work hardening through SIM) in the bulk material have negative impacts on overall performance of reactor internal structures for NPP due to their effect on sensitization to SCC [44, 45]. Hence, strengthening 300 series stainless steels by conventional processing (e.g.

cold working by rolling) is limited due to tendency of these materials to form SIM affecting their overall performance. Alternatively, improved mechanical property combinations have been reported for austenitic stainless steels due to refinement of microstructures achieved through a combination of advanced deformation routes at temperatures below the composition-dependent martensite start temperature (M_d), followed by subsequent thermal treatments, which can revert large fractions of nanoscale grains of SIM [36, 42, 46-52]. These SIM reversion based processing routes have been shown to facilitate formation of sub-microcrystalline or ultra-fine grained (UFG) microstructures with average grain sizes as small as about 0.5μm to 1μm in austenitic stainless steels, including 316 grade, and resulted in increased mechanical strength while maintaining reasonable ductility, elongations to failure [36, 42, 46-53]. Specifically, a reduction of average austenite grain size from 35μm to 330nm was achieved in 304L stainless steel through a combination of cold rolling, to produce a 100% SIM microstructure, followed by annealing, at 700 °C for 300 min, resulting in significant strengthening [53].

Plastic deformation processing routes, including severe plastic deformation (SPD) processing routes including equal channel angular pressing (ECAP) and high-pressure torsion [54, 55], have also been explored with the stated goal of exploiting grain size strengthening of austenitic stainless steels. SPD of metals and alloys, including austenitic stainless steels, typically results in a new refined microstructure, often appearing featureless in optical microscopy images, and associated with final grain sizes in the ultrafine (0.1μm < grain size < 1μm) or even nanocrystalline (grain size < 0.1μm=100nm) regimes [49, 56, 57].

Astonishing advancements in mechanical strength and ductility have been demonstrated for many materials by utilization of these alternative, and SPD based, plastic deformation processing methods [36, 42, 46-53]. However, SPD does not necessarily provide the combination

of properties or microstructural features associated with establishing improved resistance to degradation from corrosion, creep, and regarding SCC susceptibility reduction. Therefore, along with the potential practical applications of new processing routes for SPD, developing an understanding of the importance of controlling grain boundary character distribution (GBCD) and its effect on the improvement of properties in bulk polycrystalline aggregates remain an important and active area of investigation, especially for extremely grain refined microstructures that can be obtained by these less conventional or advanced plastic deformation processing routes.

2.3 PROMISE OF SURFACE MODIFICATIONS

More recently, efforts in the context of preventing surface-initiated failures have included research that intends to create materials or components where small regions of the microstructure near the surface, and near surface region, have been modified or engineered while the components' bulk microstructural parameters, which are achieved by conventional processing of flat or long product, are retained [9, 58-61]. Processes like ball or shot peening, surface mechanical attrition (SMAT), laser shock peening (LSP), and low plasticity burnishing (LPB) all impart microstructural modifications locally to the surface and subsurface regions of a material while maintaining bulk characteristics[9, 60, 61]. These processes are each used to achieve different desired effects in surface and subsurface microstructures [9, 58-61]. Through surface modification, properties such as thermal stability, mechanical strength, and degradation resistance (incl. improved resistance to fatigue, corrosion, and irradiation) could be affected beneficially by modifying only a small region of the bulk microstructure in components made

from austenitic stainless steel. Surface modification methods are capable of achieving grain size refinement, compositional homogenization by effective breakdown of heterogeneously distributed and detrimental precipitates (inclusions remaining after conventional commercial processing), and GBE [9, 31, 37, 59, 61]. In the case of processes like SMAT, SPD microstructures are created on the surface, which can improve overall mechanical behaviors[60]. Alternatively, methods like LSP and LPB create a significant amount of compressive residual stresses in the surface microstructure capable of limiting crack formation and propagation [9, 61]. While all of these methods have shown to be beneficial to the overall performance of the surface modified materials, widespread adoption has been slow. The barriers preventing large increase in the use of these methods include the overall scale of the modifications, and their repeatability, as well as the requirement to invest in large expensive apparatus, cases of non-uniform application, long treatment times, and issues with final surface finish and roughness [60-63].

2.4 LINEAR RAKING

Reduction in grain size to the sub-microcrystalline regime (average grain size below 1μm) in metals (e.g. Cu) and alloys (e.g. Al-base and Ni-base) has been accomplished by linear raking based processing, and has induced increased resistance to plastic deformation and mechanical strength[13, 14]. Furthermore, in precipitation hardenable alloy systems (e.g. Ni-base alloys) the length-scale of refined microstructures after linear raking based severe plastic deformation (SPD) processing have been shown to exhibit enhanced resistance to thermally induced coarsening

during elevated temperature exposures[14]. Importantly, an investigation of linear rake machining on titanium showed significant promise for linear raking as a surface modification technique when it was observed that surface and near-surface regions of the bulk exhibited significant evidence of deformation [14]. To date the linear raking related severe plastic deformation (SPD) processing approach has been applied to various non-ferrous alloy systems (Al, Cu. Ti) but its applicability for enhancement of surface related properties in ferrous alloys remains to be studied.

Here, as part of developing new and interesting processing techniques, a room-temperature plane-strain machining technique, was applied to 316L. Linear raking is a processing technique which uses a wedge shaped cutting tool to remove a small amount of material from a substrate, imparting large amounts of strain at high strain rates. This deformation is accomplished primarily through shear strain. Unlike other surface modification methods, the linear raking in a single path process offering controllable and repeatable characteristics for surface modifications and possible property enhancement via three principle processing parameters: the velocity of the cutting tool, the cutting tool angle and the cutting depth. Each of these main parameters can be adjusted independently. The adjustments of these three processing parameters affect the amount of total strain and the strain rate imposed on the material during linear raking [64, 65]. Therefore a wide range of deformation conditions can be explored systematically. The processing parameter control also allows for consistent application of the processing conditions over large areas of a component as well as for multiple specimens. These characteristics make linear raking an appealing process for the study of SPD in ferrous alloy systems, for which there are immediate needs for industrially scalable techniques for surface modification. Finally, it is important to note that since linear raking is a machining related

process, the wear of the cutting tool can become a significant source of variability regarding the resultant microstructures modification and process characteristics. However, this investigation used new tools for all linear raking experiments and therefore does not investigate the effects of tool wear.

Figure 1 shows a schematic drawing of the cutting geometry associated with the linear raking process [14]. The main process parameters expected to influence microstructure changes of the 316L steel in response to application of the linear raking include the tool angle, α, the linear machining or tool speed, V_c, and the depth of the cut, a_0, made by the tool into the surface of steel substrate [13, 14, 64, 65].

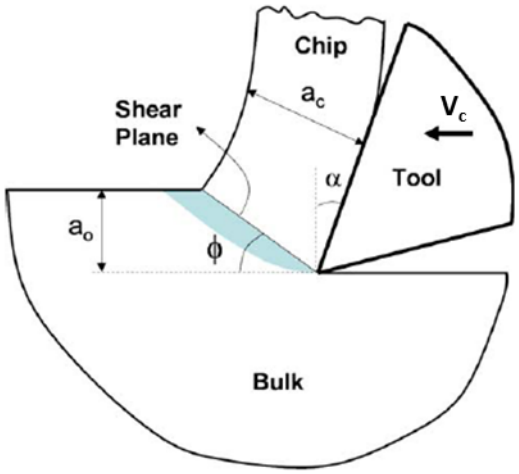

Figure 1 Schematic of linear raking [14]

In the idealized case, the deformation leading to the creation of the chip is attributed primarily to shear strain along a plane determined by the processing parameters of a_0, chip thickness, a_c, and α [65]. Once this angle is calculated an average shear strain can also be determined[65]. Therefore, by simply measuring the thickness of the chip after deformation,

which provides a_c, and the angle of the shear plane, the overall shear stain can be calculated [13, 64, 65]:

$$\tan \varphi = \frac{\frac{a_0}{a_c}\cos \alpha}{1-\left(\frac{a_0}{a_c}\sin \alpha\right)} \quad (4)$$

$$\gamma = \frac{\cos \alpha}{\sin \varphi \cos(\varphi-\alpha)} \quad (5)$$

Furthermore, the strain rate can be calculated by determining the velocity of the deformation (V_γ) by projecting the tool velocity, V_c, into the direction of the shear plane [13, 64, 65];

$$V_\gamma = V_c \cos \varphi \quad (6)$$

Then, given the length of the shear plane, L_γ [13, 64, 65];

$$L_\gamma = \frac{a_0}{\sin \varphi} \quad (7)$$

The shear strain rate, $\dot{\gamma}$, becomes [13, 64, 65]

$$\dot{\gamma} = \gamma \frac{V_\gamma}{L_\gamma} \quad (8)$$

The amount of strain, the effective strain rates, and thermal cycles experienced by the chip and those experienced by the substrate near surface region are expected to differ for a given set of

linear raking conditions. Hence, we separately studied the microstructures of both the chip and the substrate near-surface region. This enabled the assessment of the effects of the major deformation processing parameters utilized during linear raking of the 316L on the modified microstructures of the resulting chip and also the substrate near-surface regions.

3.0 OBJECTIVES

The objective of this work is to explore linear raking through a systematic investigation of the microstructures produced in the chips and substrate surfaces of 316L austenitic stainless steel and their resulting mechanical properties. Through this systematic investigation the relationships between the linear raking process parameters and the microstructural and mechanical property response of 316L austenitic stainless steel can be established. In particular, the response of both the chips and substrate surface will be evaluated. By characterizing the response of the chip, changes due to the strain and strain rates linear raking can impart, can be established in a material that has never been investigated using linear raking. This is important since the control over these principle deformation process parameters can be used in comparison with shear deformation related straining paths achieved in other plastic deformation processes. Furthermore, observing the changes imparted to the substrate surface will provide the evidence needed to evaluate and perhaps validate linear raking as a possible surface severe plastic deformation process. Using this high strain and strain rate process, it is theorized that significant property improvement could be achieved in the chips through the creation of scale refined SPD related microstructures. Additionally, it is anticipated that the deformation imparted to the substrate surface could produce surface modified, even surface SPD, structures which could be useful in designing a processing path for thermo-mechanical surface modification of austenitic stainless steels. In this way, the linear raking modified microstructures in the chips and substrate

surfaces could be utilized as the “mechanically activated” start-state for further microstructural evolution during subsequent thermal annealing treatments.

4.0 EXPERIMENTAL PROCEDURES

4.1 STAINELESS STEEL AND LINEAR RAKING SPECIMEN SECTIONING

Cold-rolled and annealed 316L stainless steel plate of dimensions 1 ft. x 1 ft. x 3/15 in. was acquired from McMaster-Carr. The nominal composition in weight percent (weight%) is listed in Table 2.

Table 2 Nominal Composition of Austenitic Stainless Steel grade 316L in weight %

Alloy	Cr	Ni	C	Mn	Cu	Mo	Si	S	P	N
316L	16.0-18.0	10.0-14.0	0-0.08	≤2.0	≤0.75	≤3.0	≤1.0	0.03	≤0.045	≤0.1

In order to facilitate processing by two-dimensional plane-strain machining or linear raking at room temperature with the experimental set-up available here at the University of Pittsburgh in the laboratory of Prof. Shankar, Department of Industrial Engineering, specimens of dimensions schematically illustrated in Figure 2 were prepared from the as-received plate. These specimens had a constant raking surface width of 3 mm and were approximately 60 mm in length. These dimensions were chosen due to the specification of the experimental raking set-up. For instance, the specimen length was determined by the size of the specimen holder, ensuring that the entirely of the work-piece fit within the holder so as to prevent excess vibrations. While the sample width was set at 3mm, as using wider dimensions for the specimen would require

larger more expensive tools and would increase the force required to drive the tool beyond the safe operating limits of the experimental raking set-up.

High-speed steel (HSS) cutting tools of differing rake angles were used to perform the linear raking process. The chips created by linear raking of these 316L specimens were typically 10 mm long by 3 mm wide, enabling preparation of reasonably sized samples for subsequent study by multiple different and complementary property and microstructure analysis techniques, e.g. discs with 3mm diameter for TEM observation could be easily obtained. The bulk or substrate (Figure 2) exhibited a linear raking modified surface region, which could also be efficiently sectioned and utilized for facile preparation of samples as required by different methods for subsequent analyses of the microstructures and for property measurements. During the linear raking the bulk specimen or substrate was held stationary by a clamping mechanism while the cutting tool is moved relative to the bulk specimen by linear translation at a constant preselected velocity, Vc, typically on the order of cm/s. With reference to the coordinate system marked in Figure 2, a cutting depth was selected by positonal height alignments of the bulk specimen relative to the tool along the direction X, and the tool was translated at the tool velocity V_c parallel the direction marked Z. The direction Y indicates a cross-sectional view of the relative arrangements of the tool and the 316L specimen.

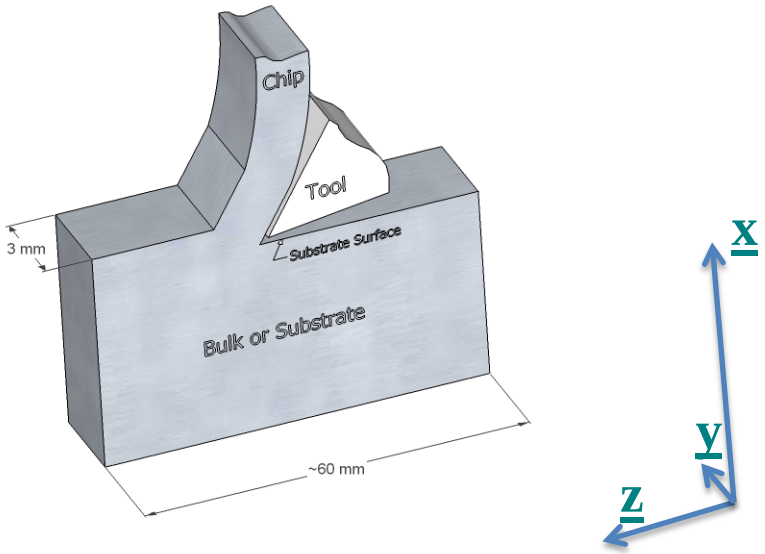

Figure 2 Diagram of work piece specimen used for linear raking experiments with characteristic dimensions

4.2 TEMPERATURE MEASUREMENT DURING LINEAR RAKING

Using an infrared (IR) camera, FLIR Systems™ Inc., model FLIR A325sc, direct measurement of the surface temperature fields evolving during linear raking was possible in real time with faster-than TV-rate acquisition at an image frame resolution of 60 frames per second, 60fps or 60Hz. Using the FLIR camera, short movie clips were recorded during raking experiments performed with different tool angles, $\alpha = 0°$ and 20°, for three different tool velocities, V_c, with V_c = 2.5 cm/s, 12.5 cm/s, and 25 cm/s, respectively. The camera specifications include a spectral range of wavelength in the thermal range of 7.5-13.0μm, a temperature range of 0 to 350 °C (± 2 °C), and an image frame capture rate of 60Hz [66]. Using this technique, the temperature

development in the chip during linear rake processing could be monitored. For these measurements the 316L bulk sample was prepared for raking as previously described and a thin layer of non-reflective black latex paint was applied to the entire specimen of 316L in order to ensure an even emissivity of the surface, allowing for accurate temperature measurement. The IR camera was then positioned to view the 316L specimen along direction of the cross-section, direction Y in Figure 2, enabling concurrent imaging of the thermal field evolution at the surfaces of the 316L substrate surface regions, the cutting tool, and the 316L chip.

4.3 HARDNESS

Micro-hardness testing has been performed using a Leco M-400-G microhardness tester with a Vickers type pyramid indenter. Microhardness measurements have been performed for the chips indenting normal to the surface defined by the length and width dimensions and also for the substrates along the normal direction, i.e., antiparallel to direction X in Figure 2, in order to monitor changes in mechanical properties. Microhardness measurements provide a simple and effective means to monitor changes in the overall strengthening effects established in the 316L microstructures of the chip and the substrate near surface regions or simply the substrate surface. The microhardness measurements can then be correlated to changes in the linear raking processing parameters, namely chiefly the cutting depth, tool angle and the tool velocity. In order to measure microhardness for the chips resulting from the linear rake processing several preparatory steps prior to the Vickers indentation testing have been performed. First, the chips were mechanically ground and then polished from both sides of the surfaces defined by the length and width dimensions using standard metallographic techniques. Namely, grinding with

600-1200 grit SiC abrasive paper and finally polishing with 0.05 μm diameter colloidal alumina in a suspension, to produce samples with smooth and parallel surfaces suitable for repeatable hardness indentation testing using the Vickers method. In order to measure hardness in the substrate surfaces modified by the linear raking, two different preparation techniques were used. First, Vickers indents were applied directly to the machined substrate surfaces along direction antiparallel to X as marked in Figure 2. Subsequently, the substrates were sectioned along the centerline parallel to the surface, defined by directions Y and X in Figure 2, ground, and polished. This enabled measurements of the changes in the microhardness as function of depth below the surface of the linear raking modified bulk substrate, i.e., depth dependent hardness profiled could be measured along the cross-sections obtained. A load of 25g and dwell time of 10 seconds were used for each condition. Ten hardness indentations were performed for each recorded measurement, rejecting the two extreme values, an average was obtained, which is then reported as the microhardness as a Vickers number [VHN].

4.4 MAGNETOMETRY

In order to determine quantitatively the volume fractions of martensite phase present in the 316L material in the as-received state prior to plastic deformation processing by linear raking and also for the 316L chips, magnetic property measurements were performed at room temperature using a Lakeshore vibrating sample magnetometer (VSM) model 7404 with a maximum magnetic field of 21.7 kOe (2.17 T) at 298K. Measurement of the saturation magnetization of each chip enables the determination of the fraction of ferromagnetic ferrite related alpha-prime martensite phase relative to that of the paramagnetic austenite phase in the 316L. Sample preparation for this

analysis required minor sectioning of the thin, ~100µm to 125µm thick, chips with width of 3mm and length of ~10mm to obtain ~3mm x 3mm cross-sectional area to fit them into the sample holder. After sectioning the thin plates obtained were carefully cleaned, weighed and demagnetized, prior to starting the scans. The externally applied magnetic field scans used a maximum magnetic field of 20 kOe (H_{max}) and involved increasing the external field from 0 kOe to H_{max} on the up-scan and then subsequently from $+H_{max}$ to $-H_{max}$ to obtain the saturation magnetization at a scan rate of 157.233 Oe/s and a step size of 0.629 kOe. Due to the small sample size needed and the effect of overall mass on magnetometry specimen preparation, reliably consistent substrate samples could not be obtained and therefore this analysis was only performed on the chips.

4.5 X-RAY DIFFRACTION ANALYSIS OF LINEAR RAKING

Using a Bruker D8 Discover X-ray diffractometer instrument with a LynxEye detector and Cu-Kα X-ray source, symmetric Bragg-Brentano XRD experiments were performed on the chips and the substrates after application of linear raking with systematically varied process parameters. The as-received state of the 316L, using the substrate surface prior to linear raking, was also analyzed by XRD to establish a benchmark for reference purposes. The investigation of chips and substrates by XRD is an effective nondestructive technique requiring relatively little sample preparation. After linear raking experiments were completed, chips and substrates were simply cleaned and degreased using acetone. The samples were then placed on a low-background silicon wafer, which was specifically cut to prevent Bragg diffraction from the Si lattice, and scans were completed using a step size of 0.02 °/step at a scan rate of 0.5 s/step. Additional scans were

conducted with the as-received 316L plate, which was sectioned, ground, and polished beforehand so as to avoid the affects that any processing might have on the surface of the as-received material, providing a reference benchmark for comparison with the linear plane-strain machined samples with their modified microstructures.

4.6 SCANNING ELECTRON MICROSCOPY

Scanning electron microscope (SEM) investigations and analyses have been performed using a Philips/FEI XL-30 FEG SEM, equipped with a field emission gun (FEG) and an orientation imaging microscopy (OIM) system from AMETEK/TSL, and a JEOL JSM-6610LV, equipped with a tungsten filament thermionic electron gun and an Oxford Instruments/HKL OIM system. Typically, the FEI XL30 FEG SEM was operated at 20kV and the JEOL JSM 6610LV was operated at 20kV. The OIM systems were used in order to characterize the microstructural modifications resulting from linear raking in both chip and substrate. The availability of multiple complimentary techniques within the SEM makes it an excellent instrument for multi-scale analysis of appropriately prepared samples. Here, secondary electron imaging (SE) and electron backscatter diffraction (EBSD) were both used as microstructural analysis tools for grain size, grain boundary and grain morphology related studies. The OIM is based on acquisition and analysis of electron backscatter diffraction (EBSD) patterns, which enables identification of crystallographic orientation with a lateral resolution on the order of about 0.2μm for the steel samples investigated. Therefore, using OIM it is possible to obtain spatially resolved data sets, i.e., not just volume averaged data as in X-ray diffraction studies, regarding phase fractions, texture, and grain misorientation, grain boundary character distribution etc.

In order to prepare the chips for analysis in the SEM, thin foil preparation was used to produce very clean, smooth surfaces, which are ideal for SEM based EBSD analysis. These foils were prepared by first mechanically punching 3mm diameter discs from the chips, which were then mechanically thinned using 600-1200 grit SiC sandpaper to a thickness between 70-90 μm, and further mechanically polished using 0.05 μm colloidal alumina. The discs were then cleaned, degreased and electrolytically polished using a Struers TenuPol Twin-Jet Electropolisher, with a solution of 73% ethanol, 10% butoxyethanol, 8% perchloric acid and 9% water at 298 K and ~20V.

The substrate samples were analyzed as cross sections. The substrate cross sections were prepared by first sectioning the substrates and mounting them in two part epoxy-resin. The mounted specimens of the substrate cross-sections were then ground using successively smaller grained (from 600-1200 grit) SiC abrasive papers, and polished using 0.05 μm colloidal alumina with final polishing accomplished on a Beuhler Vibromet vibro-polisher for 60 minutes. For SE images, the prepared substrate cross-section was then etched at room temperature with an acid solution of 10 ml nitric acid, 10 ml acetic acid, 20 ml hydrochloric acid, and 10 ml Glycerol to reveal grain boundaries and other microstructural features.

4.7 TRANSMISSION ELECTRON MICROSCOPY

For transmission electron microscopy (TEM) studies, a JEOL JEM-2100F, JEM-2000FX, and JEM-200CX were each operated at 200 kV to acquire bright field (BF) and dark field (DF) diffraction contrast images and electron diffraction patterns (DP). The TEM is an invaluable tool when characterizing highly deformed or grain refined structures due to its extremely high spatial

resolution. Additionally, the TEM's ability to quickly switch between imaging and diffraction modes at high magnifications allows for effective quantification of the highly scale refined microstructures obtained in the linear raking processed steel.

Specimens for TEM studies have been prepared for the chips as thin foils, as described previously for the SEM (section 4.6), i.e., by standard electrolytic polishing. To obtain specimens for TEM investigation for the substrates, sections were cut from the linear raking modified substrate surface, and then mechanically thinned by grinding away from only the side opposite the machined surface, the bulk-side. Then, the machined surface was masked with vinyl adhesive tape before being placed in the electrolytic twin-jet-polisher instrument (Struers TenuPol Twin-Jet) to complete the thinning. The masking prevented the electrolytic polishing and thinning away of the raked surface. The TEM foils thus obtained represent linear rake machined surface for study by TEM methods. The diagram in Figure 3 schematically depicts the relationships of the 3mm diameter discs and the electron transparent thin foil sections in them (marked as "Chip TEM sample" and "Substrate Surface TEM Sample" respectively) relative to their locations in the chip and the linear raking modified substrate surface. Hence, the TEM foils investigated here for the chips represent regions approximately located in the center of the chip, while those obtained for the substrates represent regions essentially directly adjacent to the external substrate surface that was in contact with the cutting tool during linear raking.

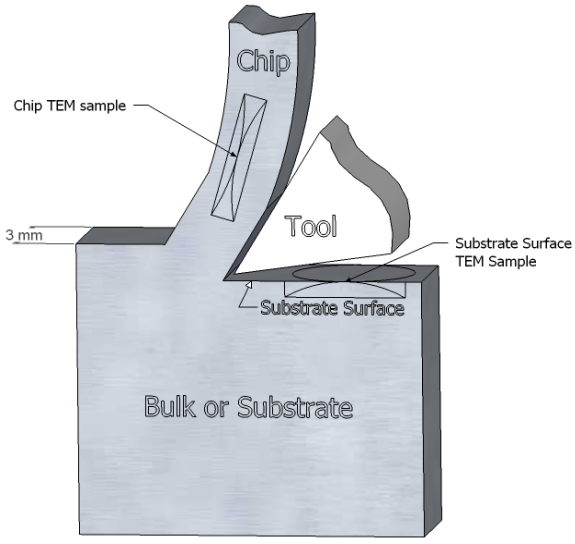

Figure 3 Diagram of how samples were sectioned and thinned from chip and substrate for TEM analysis. Note: the annotated locations and orientation so the twin-jet polished "Chip TEM Sample" and the single-side electrolytically polished "Substrate Surface TEM Sample" (see text for details)

4.7.1 Orientation Imaging Microscopy

In addition to the more conventional tilting and diffraction contrast imaging and diffraction based TEM analysis, investigations were conducted using a computer controlled system for the automated acquisition and indexing of precessed beam electron diffraction patterns in the TEM, known as ASTAR™ from NanoMegas [67]. This system incorporates both beam precession and automated scanning of the electron beam probe within the TEM in order to acquire localized precession electron diffraction (PED) patterns from predetermined areas, typically of several square micrometers in [67]. The resulting large and statistically significant PED pattern data sets can be indexed regarding their orientation and the phase they originated from with a high level of confidence dimension, due to suppression of dynamical electron diffraction effects (e.g. contrast

change due to thickness and small orientation changes) encountered in conventional parallel-beam illumination selected area diffraction [67]. Thus, using PED patterns it is possible to construct orientation maps of the areas scanned, containing information akin to the inverse pole figure maps obtained by EBSD based SEM methods of OIM. However, unlike the SEM, the TEM can attain much higher spatial resolution, only limited by the electron beam probe size at the specimen exit surface. This resolution is approximately 20 nm in a LaB_6 equipped JEM-2000FX TEM and about 3nm in the FEG equipped JEM-2100F TEM for the 316L TEM foils studied here. This TEM based OIM technique was used to produce orientation maps for the chips and substrates after application of linear raking for a variety of different processing conditions, enabling determination of local textures, grain size, grain size distribution, grain boundary character and phase fractions.

4.7.2 Profile analysis of selected area diffraction

Another analytical technique used to study the structures observed in the TEM is the profile analysis of selected area diffraction (PASAD), using a software plug-in for the GATAN Digital Micrograph™ suite of software products, utilized here for digital data acquisition and analysis of TEM data, known as the PASAD-tools [68]. This software tool allows for the quick and fully automated determination of quantitative data from TEM diffraction, by transforming the diffraction pattern by azimuthal integration into a diffraction profile similar to those acquired by x-ray powder diffraction when using a powder diffractometer type instrument, i.e., quite similar to the data in Bragg-Brentano geometry scans of intensity versus diffraction, scattering angle [68]. This TEM diffraction data analysis technique, which due to the much smaller wavelength

of the electron beam, can more accurately discern grain size and stored strain information, offers a quantitative analysis that cannot be obtained by XRD [68].

5.0 EFFECTIVE STRAIN, STRAIN RATE AND TEMPERATURE FIELDS DURING LINEAR RAKING

Using a cutting depth of a_0 = 150 μm, tool velocities of V_c = 2.5 cm s^{-1}, 6.25 cm s^{-1}, 12.5 cm s^{-1}, and 25 cm s^{-1}, for two tool angles, $\alpha = +20°$ and $\alpha = 0°$, eight nominally different plastic deformation processing conditions were evaluated regarding the effective strain, strain rate and temperature experienced by the 316L material chips during linear raking. These conditions were chosen among a variety of possible combinations of tool and tool speeds available in order to obtain reproducibly high quality specimens at a variety of strain and strain rates. Due to the nature of deformation processes, issues like tool and work piece compliance can make it difficult to calculate values for strain, strain rate and temperature of the work-piece during a particular processing path based on theoretically established models for ideally compliant systems a-priori. Therefore, direct measurements were taken to establish the plastic deformation conditions effectively imparted to the material during this two-dimensional plane strain machining process. In determining the resulting conditions of the chips an “entry zone” was taken into account, where conditions can be radically different from the rest of the chip due to compliance of the tool with the work piece when the initial piece of the chip is produced. The sections of the chip used for the analyses of the strain, strain rates were taken from regions where the chip thickness is relatively constant.

5.1 STRAIN AND STRAIN RATE FIELDS

Through direct measurements of the chip dimensions relative to the selected set of raking process conditions, such as the cutting tool angle and the depth of the cut, strain and strain rate after raking can be calculated for a given velocity of cutting (Equations 4-8, Section 2.4 and Figure 1). Table 3 shows the strain and strain rate conditions imparted to the chip for the different tool angle and tool velocity combinations applied during the linear rake processing of the 316L.

Table 3 Conditions of each raking experiment based on processing parameters and resulting chip dimensions

Tool Angle $\alpha(^\circ)$	Tool Velocity V_c (cm/s)	Cutting Depth a_0(mm)	Chip Thickness a_c (mm)	Strain γ(mm/mm)	Strain Rate $\dot{\gamma}(s^{-1})$
20	25	0.15	0.220	1.552	1273.2
20	12.5	0.15	0.253	1.698	664.3
20	6.25	0.15	0.358	2.256	356.9
20	2.5	0.15	0.371	2.338	143.6
0	25	0.15	0.195	2.073	1666.7
0	12.5	0.15	0.118	2.067	833.3
0	6.25	0.15	0.220	2.157	416.7
0	2.5	0.15	0.238	2.220	166.7

General trends regarding both strain and strain rates can be discerned for both tool angles. For instance, for the 20˚ tool angle the strain imparted to the chip decreases from about 2.3 to about 1.6 as the velocity of the cutting tool increases from 2.5cm/s to 25cm/s. Similarly, for the 0˚ tool angle the strain imparted to the chip decreases from about 2.2 to 2.1 as the tool velocity increases from 2.5cm/s to 25cm/s. So, for increasing velocity the plastic strain imparted to the

chip decreases for both the 20˚-angle and the 0˚-angle tool. However, the effect of the increasing tool velocity on the reduction of imparted plastic strain is much more significant and important for the 20˚ tool, e.g. (2.338-1.552)/1.552≈0.5 or an increase by 50% of the smaller strain, than for the 0˚ tool processing conditions, which exhibit only about 7% change from 2.22 for 2.5cm/s to 2.07 for 25cm/s. Notably, theoretical treatments predict that the plastic deformation shear strain imparted to the chip during the orthogonal machining related linear raking process is independent of the tool velocity[13, 14, 64, 65]. Hence, the experimental measurements of the chips deformed using the 20˚-angle tool, where the strain imparted to the chips decreased as the velocity was increased, indicates significant deviation the idealized behavior assumed in theoretical models. Conversely, the 0˚-angle tool conditions resulted in minor deviations from model behavior with only small differences in strain as the tool velocity was changed. Regarding the strain rates experienced by the chip a positive and direct correlation between increasing strain rate with increasing tool velocity has been revealed for both the 20˚- and the 0˚ -angle tools. Given that plastic strain imparted to the chip is almost constant for the 0˚-angle tool, the increase in tool velocity by an order of magnitude from 2.5cm/s to up to 25cm/s produced also full order of magnitude increased strain rate, namely from 167 s^{-1} to 1667 s^{-1} for the 0˚-angle tool. For the 20˚-angle tool the strain rate also increased significantly from 144 s^{-1} to 1273 s^{-1} as the tool velocity is increased tenfold from 2.5 cm/s to 25 cm/s. Finally, it appears that the overall strain that can be imparted to the chips under the different velocity tool angle conditions examined here has an upper limit of about 2.2 to 2.3 for the 316L material and selected cutting tool. Thus, the plastic strain and strain rate values associated with the plastic deformation processing by the linear rake machining for the 316L have been established by experimental measurements of the actual dimensional changes realized in the processed chips. The plastic deformation strains of

between 1.6 to 2.3 are large cold-deformations, approaching or reaching levels typical of other severe plastic deformation processes (e.g. ECAP, HPT, SMAT). The strain rates of between 144 s^{-1} to 1667 s^{-1} are very rapid when compared to more conventional cold-deformation processes (e.g. cold rolling) and severe plastic deformation processes like ECAP. Establishing experimentally the plastic deformation strain and strain rate parameters is important in the context of any further analysis of the relationships between the plastic deformation processing conditions during linear raking and resulting microstructures and properties of the 316L material, facilitating potential comparison to other plastic deformation processes discussed in the literature and therefore for benchmarking purposes.

5.2 TEMPERATURE FIELDS

Another important variable in the deformation processing of metallic alloys is the temperature at which the plastic straining occurs. This is significant because the linear raking experiments are performed nominally at room temperature and the high strain rates the process can attain imply that in some cases significant temperature elevation in excess of the nominal room temperature value could occur within the 316L material. Since temperature is an important parameter for the plastic deformation processing of metals and alloys in general and for austenitic stainless steels in particular, any excursion of the temperature to significantly elevated levels during the thermo-mechanical cycle of the 316L chips and the bulk substrate experienced during the raking process can potentially significantly alter the resulting microstructures. For austenitic stainless steels the potential for and role of plastic deformation strain induced martensite (SIM) sensitively depends on the deformation temperature, since the effective SIM start temperatures, M_S and/or

M_d(30/50), are typically in the vicinity of, or below, room temperature [36, 42, 55]. Hence, here the thermal cycles experienced by the 316L work-piece during the linear rake machining process have been determined to assess boundaries for the effective plastic deformation processing temperatures for the various tool angle and velocity combinations examined.

Using the strain and strain rate data collected, the overall temperature rise in the chip can be estimated through calculation. By coupling the work done by plastic deformation during the linear raking process to the temperature at the shear plane, the overall rise in temperature can be calculated [69].

$$\rho C_p dT = (1-\beta)\, \sigma(\varepsilon,\dot{\varepsilon},T)\, d\varepsilon \quad \textbf{(9)}$$

The equation above describes that for an increment dε in strain there is an equivalent dT temperature. Here ρC_p is the heat capacity of 316L stainless steel and $\sigma(\varepsilon,\dot{\varepsilon},T)$ is the Johnson-Cook model for describing flow stress as a function of strain, ε, strain rate, $\dot{\varepsilon}$, and temperature, T [70]. The calculated flow stress is then multiplied by (1-β), where β is a factor for determining the fraction of the heat transported away from the chip by the workpiece during linear raking[71]. The factor β is given by:

$$\boldsymbol{\beta = \frac{1}{4\alpha} erf\sqrt{\alpha} + (1+\alpha) erfc\sqrt{\alpha} - \frac{e^{-\alpha}}{\sqrt{\pi}}\left(\frac{1}{2\sqrt{\alpha}} + \sqrt{\alpha}\right)} \quad \textbf{(10)}$$

Where α is a function of the raking parameters V_c and $a_{0,}$ the shear angle ϕ, and the thermal diffusivity of the workpiece κ [69]:

$$\boldsymbol{\alpha = \frac{V_c\, a_0 \tan \varphi}{4\kappa}} \qquad \textbf{(11)}$$

By rearranging these expressions the total temperature rise can be determined by the integral [72];

$$\boldsymbol{\int_{T_0}^{T_{calc}} \frac{\rho C_p(T)}{1-\left(\frac{T-T_r}{T_m-T_r}\right)^m} dT = (1-\beta)\left(A\varepsilon + \frac{B}{n+1}\varepsilon^{n+1}\right)\left(1 + C\, ln\left(\frac{\dot{\varepsilon}}{\dot{\varepsilon_0}}\right)\right)} \qquad \textbf{(12)}$$

Where A, B, C, $\dot{\varepsilon_0}$, *m* and *n* are material constants determined through a combination of analytical and empirical techniques by Chandrasekaran *et al.* [73],and where T_m and T_r are the material melting temperature and room temperature respectively [70]. Using these equations it is possible to theoretically evaluate the maximum temperatures that can develop in the chips. The results of these calculations are collected in Table 4 below.

Table 4 Maximum calculated temperatures of chips during linear raking

Tool Angle α(°)	Tool Velocity V_c (cm/s)	Strain γ(mm/mm)	Strain Rate $\dot{\gamma}(s^{-1})$	CalculatedTemperature T_{calc}(°C)
20	25	1.552	1273.2	201
20	12.5	1.698	664.3	161
20	6.25	2.256	356.9	138
20	2.5	2.338	143.6	97
0	25	2.073	1666.7	253
0	12.5	2.067	833.3	193
0	6.25	2.157	416.7	152
0	2.5	2.22	166.7	106

From these results it is clear that strain rate is the primary factor in determining the maximum temperature experienced by the chips during linear raking. As a result of this strain rate sensitivity, the chips formed using the 0° angle-tool should develop higher temperatures than those formed using the same velocity but with the 20° angle-tool. Finally, the temperatures calculated here range from about 100 °C to 250 °C , which are well above the compositionally dependent values for significant martensite formation during cold working $M_{d(30/50)}$, where $M_{d(30/50)}$= -33˚C (≈240K), and therefore significantly reduced martensite content can be expected to result in the linear raking processed 316L.

Thermal imaging, with IR thermography, was used here to experimentally determine the temperature fields evolving during the linear raking process. Using a forward-detecting infrared camera the temperature of the chips and bulk substrate surface region could be examined in real time. Figure 4 shows examples of thermal images collected during linear rake machining using both the 0° and 20° tool angles at three different velocities, 25 cm/s, 12.5 cm/s and 2.5 cm/s, respectively. The frames shown are those for which the maximum chip temperatures have been observed for the six different deformation processing conditions. In determining the maximum chip temperature, the “entry zone” effect was taken into account, and therefore the part of the chip initially formed when the tool first comes in contact with the work-piece was disregarded. The maximum temperature was obtained from the regions of constant chip thickness well after the initial tool to work-piece contact had been established.

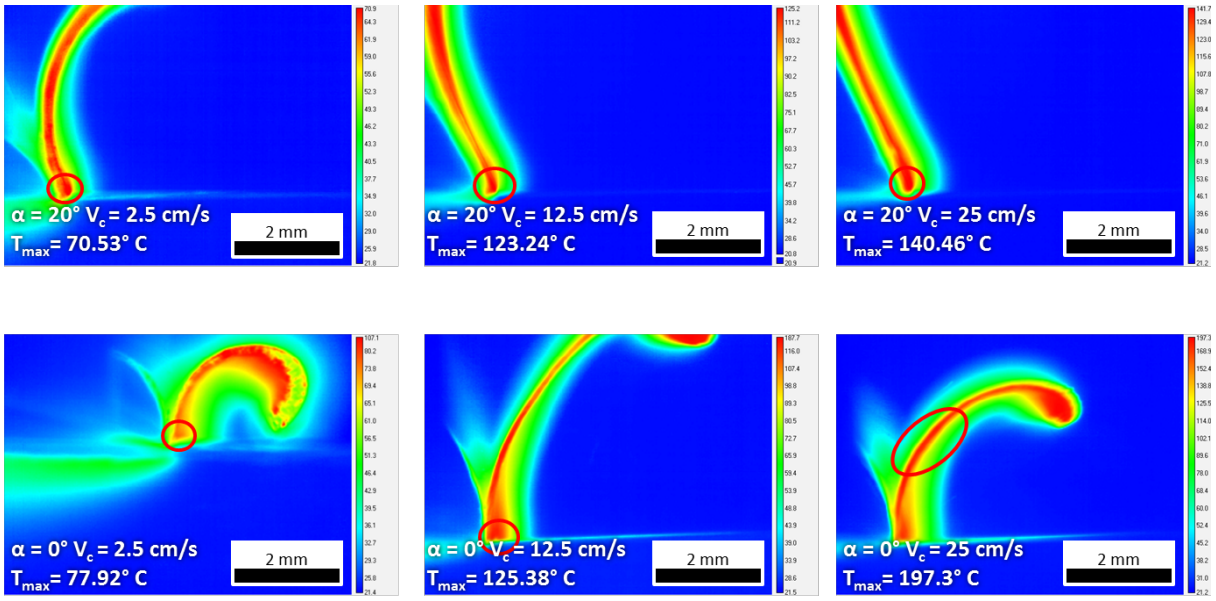

Figure 4 IR-camera images showing temperatures fields during linear raking (peak temperature highlighted in red)

Generally, the maximum temperature observed was measured in close proximity to the tool-chip contact interface and ranged from about 70˚C (≈343K) for the small strain rates associated with the 2.5cm/s tool velocity up to about 197˚C (≈470K) for the very highest strain rates associated with the 25cm/s tool velocity (Figure 4). An exception was observed for the case of a tool angle $\alpha = 0°$ and the high velocity $V_c = 25$ cm/s, where the peak temperature occurs at a location away from the tool-chip interface further up in the chip (Figure 4, region marked by the oval). While this is the only condition where the true maximum is not at the tool interface, other conditions involving the higher tool velocities of 12.5cm/s and 25cm/s, including the case of $\alpha = 0°$ and $V_c = 12.5$ cm/s, also showed local temperature maxima at locations away from the tool-chip interface region, see Figure 5. Comparing the temperatures measured using IR-Thermography to the calculated temperatures for martensite formation, M_s and $M_{d(30/50),}$ where $M_s < 0$ K and $M_{d(30/50)} = -33$˚C (≈240K), is it clear that the temperatures experienced by the chips

during the linear raking process are significantly higher than these SIM formation temperatures. The temperatures calculated using Equation 12 were of the same order of magnitude as those measured by thermography. However, the experimentally determined chip temperatures were consistently and systematically smaller than the theoretically predicted values. For instance, in the cases of the smallest and largest chip temperature rise the ratios of $\Delta T_{exp}/\Delta T_{calc}$ are (47/77)≈0.64 and (174/230)≈0.75 respectively. Hence, the experimentally observed temperature increases associated with the linear raking process are qualitatively and even quantitatively in reasonable agreement with the theoretical predictions.

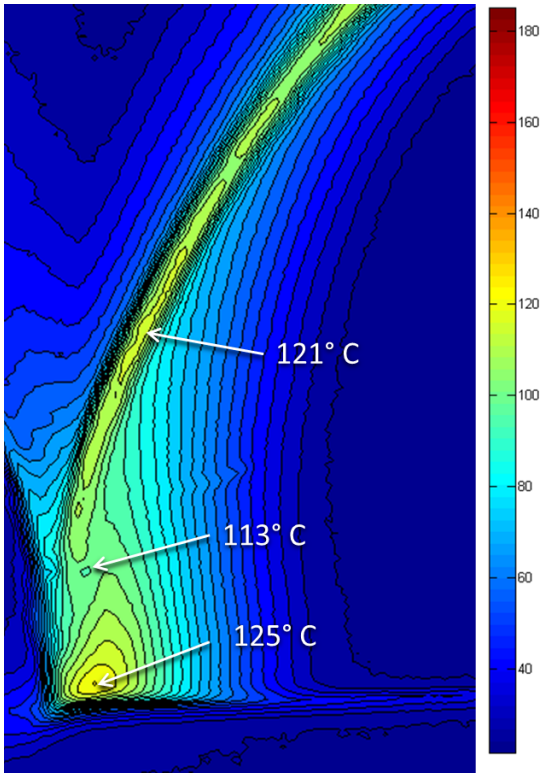

Figure 5 contour map showing chip temperature ($\alpha = 0°$ and $V_c = 12.5$ cm/s) and local maxima away from the chip tool interface (contour lines represent 2° C change in temperature)

Consistently, it was observed that the faster the tool speed, V_c, results in the higher the maximum observed temperature. Also, the chips formed using the 0°-angle tool consistently exhibited a higher temperature than the chips formed with the 20°-angle tool. The thermal images collected with the IR-camera system clearly indicate that the maximum temperature experienced by material volumes in the 316L chips increases with increasing tool velocity, and therefore with the strain rate measured in the chip. Given that the chips formed using the $\alpha = 0°$ tool exhibited only small variations of up to about 7% in the total shear strain imparted to them for the full range of strain rates ranging over about one order of magnitude from 166 s^{-1} to about 1667 s^{-1} (Table 3, above), it can be concluded that the maximum material temperature in the chip increases with increasing strain rate. Comparing the temperature fields in the chips in more detail, the development of the secondary local temperature maxima further away from the tool-chip interface of the chips deformed with the $\alpha = 0^{\circ}$ tool at 2.5cm/s and 12.5cm/s ($\gamma = 2.2$ and 2.1 and $\dot{\gamma} = 166$ s^{-1} and 833 s^{-1} respectively) can be identified as the major quantitative and qualitative difference. Of course, on average the maximum temperatures developing in the 316L chip were higher for the higher strain rate conditions, namely $T_{max} \approx 126^{\circ}C$ ($\approx 400K$) for the strain rate of 833 s^{-1} and $\approx 78^{\circ}C$ ($\approx 352K$) for the 166 s^{-1} strain rate. The frictional interactions at the contact surface between tool and chip are the main sources for the increased temperature in the chip and are due to the contact mechanics of the linear rake machining process. Hence, the machining process related heating of the chip material originates at locations near the temperature maximum observed in close proximity of the tool-chip interface. While numerical modeling of the heat transfer process in the chip has not been performed, it appears reasonable to propose that simple continuum models including the radiation and solid state transport for the dissipation of the linear rake machining process heat cannot easily predict the observation of the

local temperature maxima far away from the frictionally heated tool-chip interface regions, further up in the chip[74]. Hence, it is tempting to speculate or hypothesize regarding the origin of these local subsidiary temperature maxima. One potential origin for the subsidiary and localized temperature maxima that could be proposed would be the occurrence of exothermic solid state reactions in the plastic deformation modified chip microstructure, such as recovery processes, reversion of SIM and recrystallization, which would be releasing heat as the deformed structures locally rearrange and evolve to reach lower energy states after the plastic shearing in the process zone near the contact with the tool.

5.3 CONCLUSIONS

The results presented here show that using linear raking a wide range of plastic deformation (strain, and strain rate) conditions can be achieved with relatively little change in the overall setup. The experimentally determined actual plastic strain and associated strain rate obtained in the chip by linear rake machining ranged from strains of about 1.6 to 2.3 with strain rates up to about 1700 s^{-1}, while local temperatures reached as high as about 200˚C (473k) for some plastic deformation processing conditions. The total strains are large and accomplished at very rapid rates, enabling access to a broad spectrum of plastic deformation conditions by relatively easily effected adjustments of the tool speed and tool angle. Additionally, the measured temperature fields evolving in the chips and substrate near surface regions, inclusive of the observation of the local temperature maxima at locations away from the tool, provides important information about how the microstructures in the chip may be responding to the plastic deformation imparted by linear raking. These subsequent local temperature maxima would appear to be consistent with

continued release of the energy imparted by the plastic deformation process in the chip well after the raking tool has passed. This might signify continuous recovery of the microstructures after the deformation from the tool has been completed. It can then be surmised from these results that some of these high strain rate conditions are capable of producing at least somewhat stabilized or relaxed microstructures. Therefore, further investigation into the microstructures of the chips after deformation is necessary.

6.0 EFFECT OF RAKING ON CHIPS

In this section, the overall effects of the primary linear raking process parameters, the cutting tool velocity (or speed) and tool angle, on the resulting properties and microstructures in the 316L austenitic stainless steel chips produced were studied. By first exploring the effects of linear raking on the chips the microstructural and property response of 316L due to the high strain and strain rates imparted to the chips can be observed and measured quantitatively. Additionally, the grain refined SPD microstructures observed in the chips produced using other materials can be verified for 316L.

For this investigation, the depth of cut, a_0, was kept constant, a_0 = 150 μm, while two different tool angles, α=20˚ and 0˚, were combined with four different tool velocities (V_c = 2.5, 6.25, 12.5, 25.0 cm/s).These conditions were chosen among a variety of possible combinations in order to obtain high quality specimens at a variety of strain and strain rates. By combining XRD, SEM, TEM, magnetometry and microhardness, the microstructural changes in 316L chips due to the deformation resulting from processing by 2D plane-strain machining have been evaluated. The goal of the following sections is to present the respective experimental results in order to support the development of an understanding of the relationships between the linear raking (two-dimensional plane strain machining) processing parameters, and the resulting microstructural and property evolution in 316L. Notably, changes in cutting tool velocity and/or angle for a constant depth of cut during two-dimensional plane strain machining essentially facilitate exploration of

the effects of changes in the apparent total strain, the effective strain rate and temperature the chip is exposed to in this themo-mechanical process.

6.1 EFFECT OF TOOL VELOCITY ON CHIPS

In order to assess the effects of the tool angle, four different tool velocities, namely 2.5cm/s, 6.25cm/s, 12.5cm/s and 25cm/s, have been utilized in a comparison for two different tool angles, namely $\alpha = 20^{\circ}$ and $\alpha = 0^{\circ}$. Figure 6 presents symmetric Bragg-Brentano XRD scans obtained for the chips created using two different tool-angles, 0° and 20°, for the four different tool velocities and the as-received material as a reference benchmark. The as-received material had a grain size of approximately 20 μm and exhibits the signature XRD peak positions and intensity ratios typical for austenitic 316L stainless steel with high-intensity face-centered cubic (fcc) peaks, associated with γ-phase austenite, and a low-intensity body-centered cubic (bcc) 110 peak characteristic of the strain induced martensite (SIM) phase, the bcc related α'-phase, typically considered to have a tetragonal structure. Changes in the relative intensities of the I_{111}/I_{200} and I_{111}/I_{220} peak ratios of the majority austenite phase in the scans of the plane-strain machining deformed samples indicate a deformation-induced change in texture. Peak area analysis, involving deconvolution of the austenite (I_{111}) peaks from the martensite (I_{110}) peaks, indicates significant changes, which would be consistent with an increase in the martensite (SIM) volume fraction in response to the plastic deformation processing. Finally, the plane-strain machining modified microstructures of the chips exhibit significant peak broadening in the respective XRD scans, which can be attributed to either grain size refinement ($D_{grain} < 100$ nm) or stored strain from the plastic deformation processing [75].

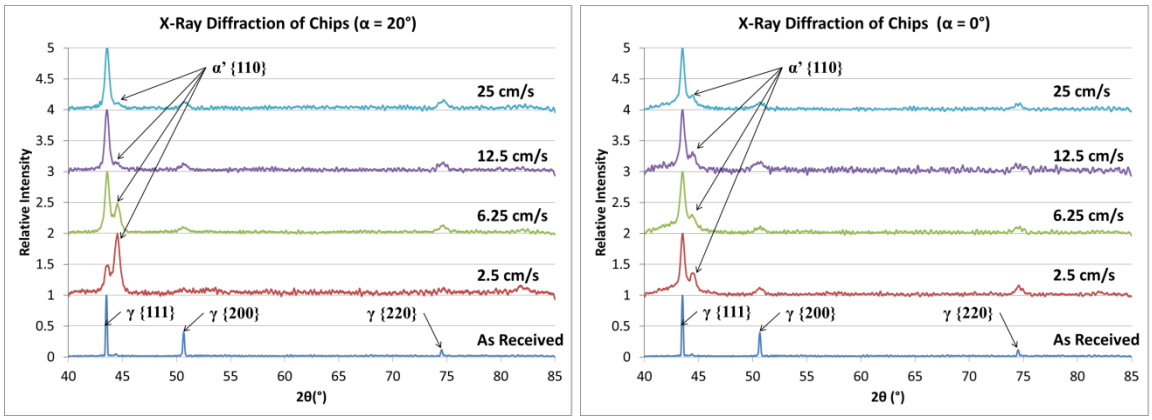

Figure 6 XRD scans of chips creating using 2 tool angles (α) and 4 tool velocities (V_c), showing texture change through variation in peak intensity, as well as martensite volume fraction through increase in α'(I_{110}) peak intensity

In conventional cold deformation processing, e.g. cold-rolling at room temperature, the volume fraction of SIM expected after an amount of deformation strain equivalent to that imparted to the chips by the plane-strain machining operation, i.e., strains after ~80-90% cold rolling reduction, would be expected to be on the order of ~20% [8]. Based on the XRD peak area analyses using the strongest austenite and martensite phase peaks, i.e., I_{111} for the austenite and I_{110} for the martensite, Table 5 shows that the experimentally measured SIM (α'-phase) volume fraction increases from ~0.5% in the case of the as-received material to values of ~2% for the faster tool speeds, e.g. 12.5 cm/s ≤ V_c ≤ 25 cm/s. The XRD data based analysis indicates that the highest SIM content was observed for the tool angle and velocity combination of α = 20° and V_c = 2.5 cm/s, with α'-martensite volume fraction reaching 40%. However, the XRD peak intensity based analyses performed here may not be representative of the true volume fractions of the phases throughout the volume of the plastic deformation processed chip material. Extracting quantitative volumetric phase fractions from polycrystalline aggregates after plastic deformation

processing using XRD has inherent limitations. Primarily, the development of crystallographic texture can have significant effects on the overall intensity of the observed diffraction peaks, rendering them unreliable for use in attempts of phase fraction determination, especially when data analysis is limited to singular or small numbers of phase specific peaks [76]. Also of importance in evaluating the effectiveness of XRD in measuring phase volume fraction changes are the limitations arising from attenuation of Cu-Kα radiation by iron atoms in the steel, limiting the depth of the region of chip material probed by the X-ray beam to a maximum of ~14 μm in depth below the external surface for an incident beam angle of 90° [75]. Notably, at normal incidence, 90˚, the maximum penetration depth for the X-rays that are detected in the XRD scans is achieved [70]. Hence, here, XRD may be considered a surface sensitive technique since the about 10-14μm thick regions probed correspond to a relatively small fraction of the chips produced by the liner raking, which are on the order of 120 to 370μm thick in cross-section. Figure 7 compares XRD scans taken from the opposing surfaces of the chips created using a tool angle of 20°, in order to elucidate whether differences exist and might correlate with the different stress states. For these scans, both sides of each chip, the side exposed to air during the raking process (air-side) and the side interfacing with the cutting tool (tool-side) were investigated by equivalent XRD scans and then overlaid to enable direct comparison. Notably, the opposing sides are nominally under opposite sign effective residual stress states, tension on the air-side and compression on the tool-side. The shifts in the relative peak psoisiont of the primary (strongest) peaks in the associated data (Figure 7) are consistent with the residual stress states being of opposite stress states for the opposing surfaces of the chips. Therefore, differences in the overall strain experienced by the chip through the cross-sectional thickness are to be expected.

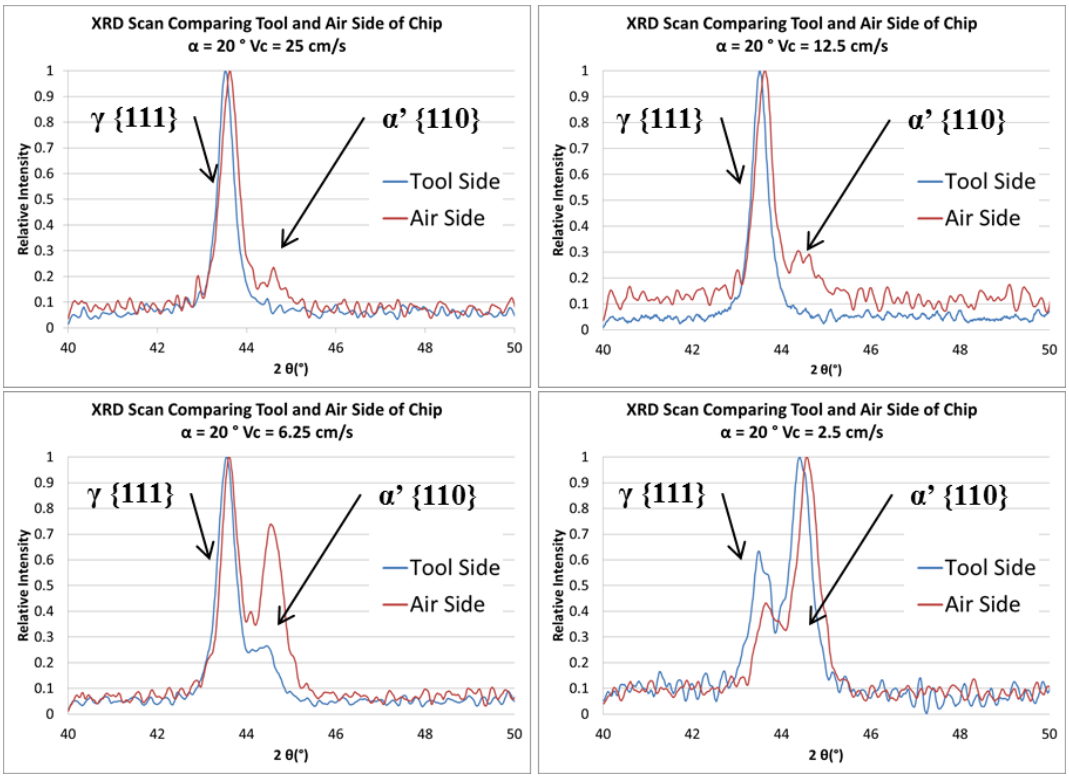

Figure 7 XRD Scans comparing the $\gamma(I_{111})$ to the $\alpha'(I_{110})$ peaks on either side of the chips created using the $\alpha = 20°$ tool at four velocities. For each chip the 'tool side' and 'air side' are overlaid on the same chart.

Some intensity due to martensite phase (SIM) can be identified in some of the XRD scans for each of the chips (Figure 7). However, for the tool side scans there are no discernible peaks associated with SIM in the two high-speed raking experiments (12.5 and 25 cm/s). Also, in all cases the intensity of the martensite peak, I_{110}, is higher for the air-side of the chip than for the tool-side of the chip when normalized to that of the respective austenite peak, I_{111}. This trend in the SIM fraction development would be consistent with the expected effects of the temperature profile developing in the chip during the deformation process. A gradient in temperature might be expected across the chip cross-section, where the air-side remains always at lower

temperature than the tool-side of the chip. This would seem to hold the most true in the cases of the higher velocity (12.5 and 25 cm/s) raking experiments where contact area with the tool appears to be higher and friction results in higher temperatures (Section 5.2). Comparison of the XRD scans from the two opposing chip surfaces therefore indicates that a gradient exists for the martensite (SIM) volume fraction through the thickness of the chips. The differences in the relative heights of the γ{111} and the α'{110} for the opposite sides of the chip combined with the presence of only a single α'-martensite peak and the texture induced relative peak intensity changes, suggest that it is inappropriate to use solely the XRD peak area analyses method in attempts to determine accurately the evolution of the volumetric phase fractions of SIM during the deformation processing of the 316L chips [75]. Therefore, as an alternative to the XRD experiments, the relative phase fractions of the ferromagnetic α'-martensite phase present in the austenitic 316L steel samples has also been determined by magnetometry measurements using a vibrating sample magnetometer (VSM). The volumetric phase fraction of the ferromagnetic SIM phase is determined by measuring the saturation magnetization, M_s, of the chips and comparing these measurements with a reference of a fully ferromagnetic standard [77]. The SIM volume fractions obtained for the 316L material as a function of tool velocity and tool angle obtained from the XRD data analyses and the VSM measurements are summarized in Table 5.

Table 5 Martensite volume fraction as determined by X-Ray diffraction and VSM in chips produced by linear raking at eight different conditioons

Tool Velocity	Volume Fraction of α' in chip (α = 20°)		Volume Fraction of α' in chip (α = 0°)	
V_c (cm/s)	XRD	VSM	XRD	VSM
25 cm/s	1.79%	1.55%	6.19%	3.61%
12.5 cm/s	2.41%	2.35%	7.42%	3.30%
6.25 cm/s	10.97%	2.89%	6.68%	3.53%
2.5 cm/s	40.44%	3.09%	10.53%	9.20%

The VSM measurements represent truly volumetric data regarding the SIM fraction for each of the chips. In all cases the XRD data analysis resulted in elevated levels of SIM in the samples relative to the VSM measurements. This would be consistent with a gradient in SIM fraction through the thickness of the chips. The XRD scans probe the near surface regions of the chips to a depth of about 14 μm, which apparently exhibit an elevated SIM fraction relative to the volumetric average determined by magnetometry. This effect appears to be most pronounced for the combination of the lowest tool velocity, 2.5cm/s, and the 20˚ tool angle. Consistently and for both tool angles, the effect of increasing tool velocity is to reduce the differences between the XRD and VSM experiment based measurements for the SIM fractions in the 316L chips. An increase in the tool velocity reduces the amount of SIM present in the chips obtained by two-dimensional plane strain machining. The overall SIM (α'-phase) fraction measured in the 316L chips by VSM, ranging from about 1.6% to 9.2%, is lower by at least a factor of two and up to an order of magnitude than would be expected based on experience with more conventional room temperature deformation processing of the 316L steel [8]. This may be taken as evidence for the ability to use linear raking (two-dimensional plane strain machining) for imparting significant strain to 316L chips without the formation of significant SIM. For both tool angles, α = 20° and

0°, the SIM fraction increases as the tool speed is decreased. Conversely, also the SIM fraction decreases as the tool speed increases. This correlates qualitatively with the expected evolution of the plastic deformation induced temperature in the chip, since increase in the local chip material temperature for the higher tool velocities would be expected to result in reduced tendency to form SIM (Section 4.2). The chip temperature increases for plane-strain machining deformation at higher speeds. This assists in suppressing the formation of SIM. α'-martensite is expected to form at or above a critical amount of strain during plastic deformation processes at temperatures below a strain path and material composition dependent SIM start temperature [38]. Finally, the consistently larger martensite volume fractions obtained from the XRD may indicate that the martensite volume fraction in the region near to the surface of the chips is elevated relative to the average volume fraction and locations farther from the surface towards the chip interior. Such a gradient in SIM content through the chip thickness may be related to the enhancement of effects from interactions with the tool for the near surface regions of the chip and details of how heat is developed and then lost during thermo-mechanical cycle associated with the two-dimensional plane strain machining process. Thermography measurements typically indicated that the highest temperatures in the center of the chip cross-sections and lower temperatures at the surfaces (see Figure 5). The experimental data obtained for the SIM fraction evolution for the different linear raking conditions is consistent with the temperature field evolution data obtained for equivalent conditions. As the temperature rise experienced by the chip increases, generally corresponding to an increase in strain rate, a lower measured martensite volume fraction results. This observation is consistent with the fact that the amount and stability of martensite produced during deformation is dependent on the strain rate and temperature at which the deformation occurs [8, 34, 35].

Mechanical property measurements were performed for the chips using Vickers microhardness indentation. Figure 8 summarizes the hardness measurement results for the chips formed for the eight different linear raking conditions. The microhardness of chips correlates generally to the tool angle and the strain measured. Interestingly, the tool speed, and perhaps by extension also the martensite (SIM) volume fraction, appear to have much less significant effect on the measured hardness. For instance, for the 0˚-tool angle the microhardness values for the chips obtained for the slowest, 2.5cm/s, and fastest, 25cm/s, tool speeds remains constant within the margin of error, and the same holds for the chips machined with a tool angle of $\alpha = 20°$. Hence, it can be concluded that correlation of the microhardness with the strain imparted is strong, while correlation with the strain rate is weak.

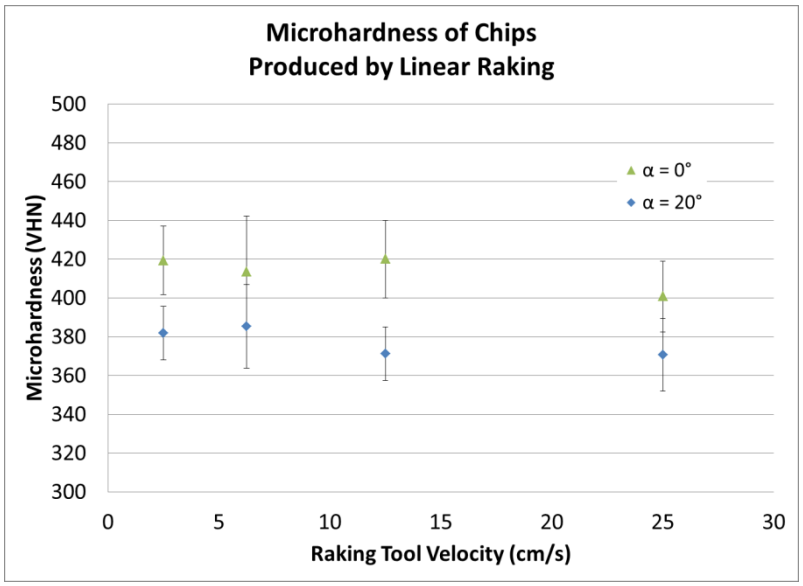

Figure 8 Hardness of chips created using $\alpha = 0°$ and 20° at 4 different velocities (2.5, 6.25, 12.5 and 25.0 cm/s)

Initial microstructural investigation by the SEM yielded very little useful information regarding the plane-strain machining induced microstructural changes in the chips due to the large degree of plastic deformation and the associated large scale reduction (refinement) of the resulting microstructural features, e.g. austenite or martensite phase grain size. For example, Figure 9 compares inverse pole figure (IPF) orientation maps obtained by SEM EBSD based OIM for the as received state and the chip microstructures after linear raking. In Figure 9a the as-received microstructures shows grains of about 20 μm diameter which are clearly identified and successfully indexed regarding their respective orientation. Figure 9a and 9d show orientation maps obtained with the much higher lateral spatial resolution for the chip microstructures after linear raking using the 20˚ and 0˚ tool angles and a tool velocity of 12.5cm/s. Figure 9c and 9d clearly illustrate the limited utility of these later data sets, since only very small fractions to none of the voxels are successfully indexed regarding orientation. The SEM experimentation indicated that visualization and probing of the scale of the relevant features of these microstructures required spatial resolution on the order of nanometers, i.e., the use of TEM based methods. Figure 10 and 11 show examples of representative TEM BF and corresponding large field of view SAD diffraction patterns of the microstructures of chips using $\alpha = 0°$ and 20° for a range of tool velocities.

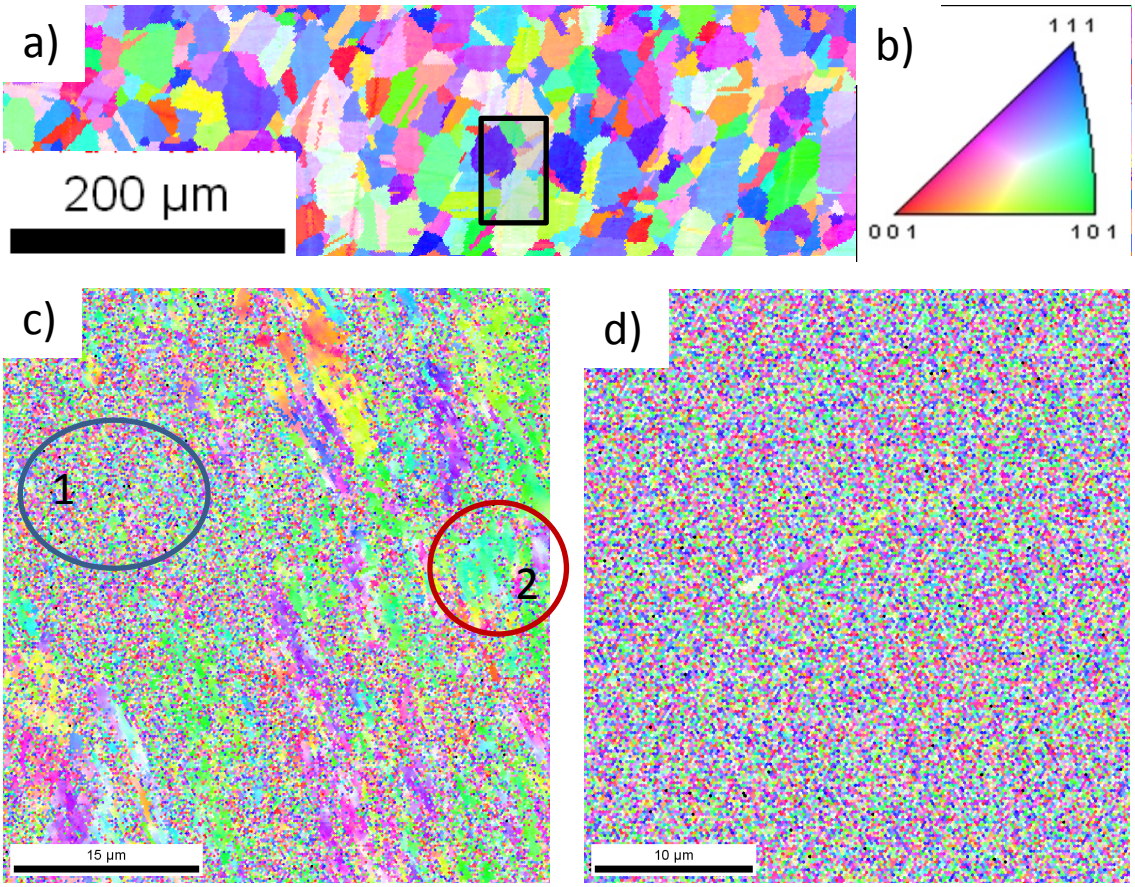

Figure 9 SEM EBSD based inverse pole figure (IPF) maps obtained for a) the as-received 316L, b) the color-coded IPF orientation legend, and chips created using c) $\alpha = 20°$ and d) $\alpha = 0°$ at 12.5 cm/s. The rectangle in b) marks a region of the scale of the IPF maps in c) and d). The regions circled in c) represent regions where orientation indexing failed, label 1, and with barely acceptable confidence succeeded, label 2.

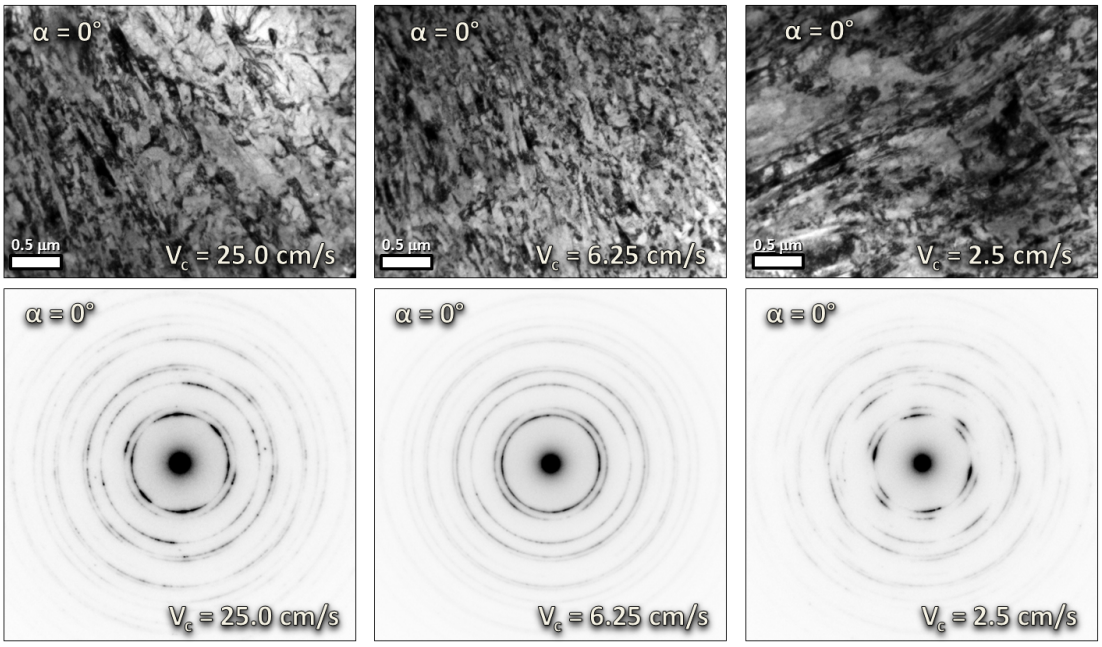

Figure 10 Representative TEM BF and DP of chips created by linear rake machining at multiple velocities (α = 0°)

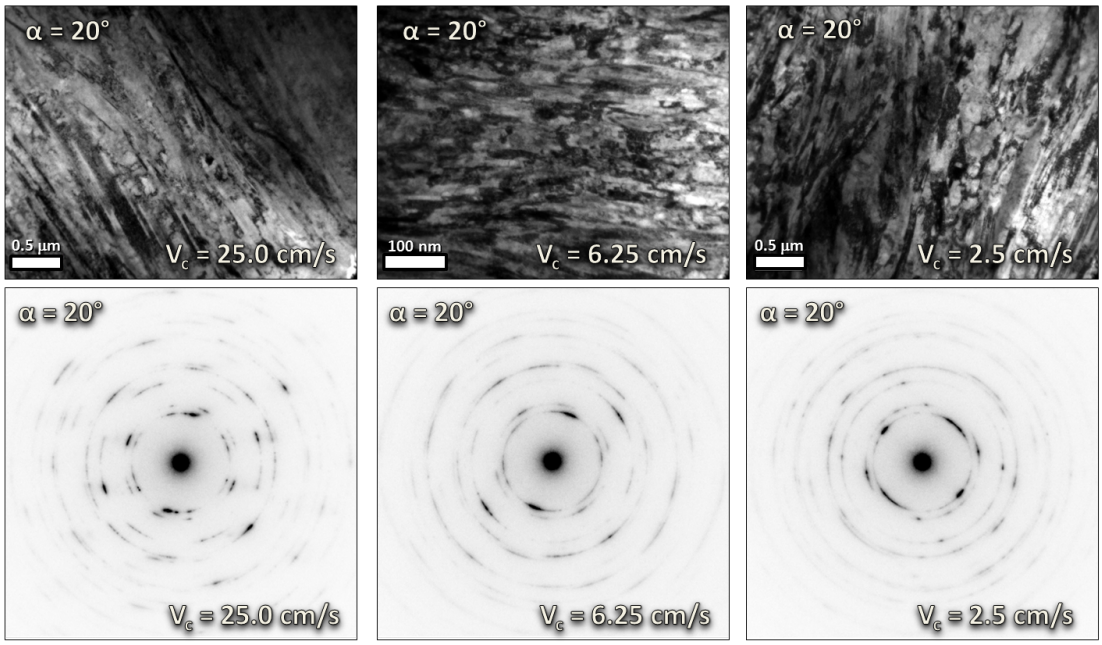

Figure 11 Representative TEM BF and DP of chips created by linear rake machining at multiple velocities (α = 20°)

Figure 10 and 11 show representative examples of the TEM bright field (BF) micrographs and corresponding selected area diffraction patterns (SADP) of the microstructures created in the chips by raking at three different velocities for the 0˚-angle tool and the 20˚-angle tool respectively. In all cases, the microstructures formed after linear raking in the chip are reduced in scale, from the 20 μm grain size observed in the as-received material, to the sub-micron and/or nanometer scale range. Depending on the raking condition, however, some notable differences are observed. Since the overall plastic strain and the microhardness measured in each of these conditions is about the same, the differences in the microstructures reflected in the TEM imaging and diffraction data can be attributed mainly to the differences in raking velocity and the associated change in strain rate. In the case of plane-strain machining with a velocity of 2.5 cm/s, the microstructures observed in the BF TEM micrographs and the corresponding diffraction patterns for both tool angles are very similar (Figure 10 and 11). In these BF micrographs the contrast arises from a variety of sources, including crystal lattice orientation changes, grain orientation, sub-grain misorientation, stored strain, and the strain fields associated with crystalline defects [78]. Here contrast related to stored strain, in particular large areas of mottled contrast which are indicative of a high dislocation density, is observed in the BF images for the chips deformed with a tool velocity of 2.5 cm/s (Figure 10 and 11) [78]. The corresponding SAD patterns collected from the areas viewed in the BF images are critical in analyzing and interpreting the BF image contrast. The SAD patterns collected for the 2.5 cm/s chips exhibit spot type patterns. These types of SAD patterns are formed when only a small number of discrete volumes of the sample with different orientations diffract the incident electron beam, creating intensity in well-defined and discrete locations along the rings of constant scattering angle. This signifies that only a few differently oriented grains contribute to

the intensity maxima in these patterns. Therefore, only a few different grains are present in the selected field of view of the corresponding BF images [78]. Further analysis of these SAD patterns reveals that the diffraction maxima exhibit discernible radial (Δk) broadening parallel to the corresponding diffraction vector (g-vector) and also some azimuthal ($\Delta\theta$) arcing, which are characteristic features of stored inhomogeneous or non-uniform strain (e.g. dislocations in sub-grain cell structure walls) and small sub-grain cell misorientations of up to $\sim 3^{\circ}$. These characteristics are consistent with the formation of a heavily cold-deformed cell structure within larger grains. Therefore, from analysis of these images and corresponding SAD patterns it can be concluded that a scale refined and heavily deformed microstructure appears to be present in these samples. As the velocity is increased the differences in strain rate, between deformation applied using 0° and 20° angle tools, also increases (see Section 5.1). Correspondingly, the microstructures begin to differ more significantly. In particular, a larger number of considerably smaller grains are imaged in BF TEM micrographs for the 0° tool-angle chips than in the 20° tool-angle chips obtained for the same tool velocity, e.g. 2.5 cm/s and 25 cm/s. This can be confirmed by comparing the associated SAD patterns. Figure 12 below shows a direct comparison of the SAD patterns collected from the chips produced at 25.0 cm/s using the 0° and 20° raking angle tools. Examining Figure 12 it is evident that more complete diffraction rings are present in the case of the 0° tool-angle chips than for the 20° tool-angle chips. This is indicative of a large number of individual grains that are significantly misoriented with respect to each other in the 0° tool-angle chips and signifies dramatic grain size refinement. In comparison, the SAD patterns from the 20° chip materials exhibit a more discrete intensity distribution along the rings associated with the diffraction angles associated with the {111}, {200}, {220}, etc. planes

of the FCC γ-phase. Hence, fewer grains are present in the BF image fields of view for the 20° chip produced at 25 cm/s tool velocity than in the 0° chip produced at the same velocity.

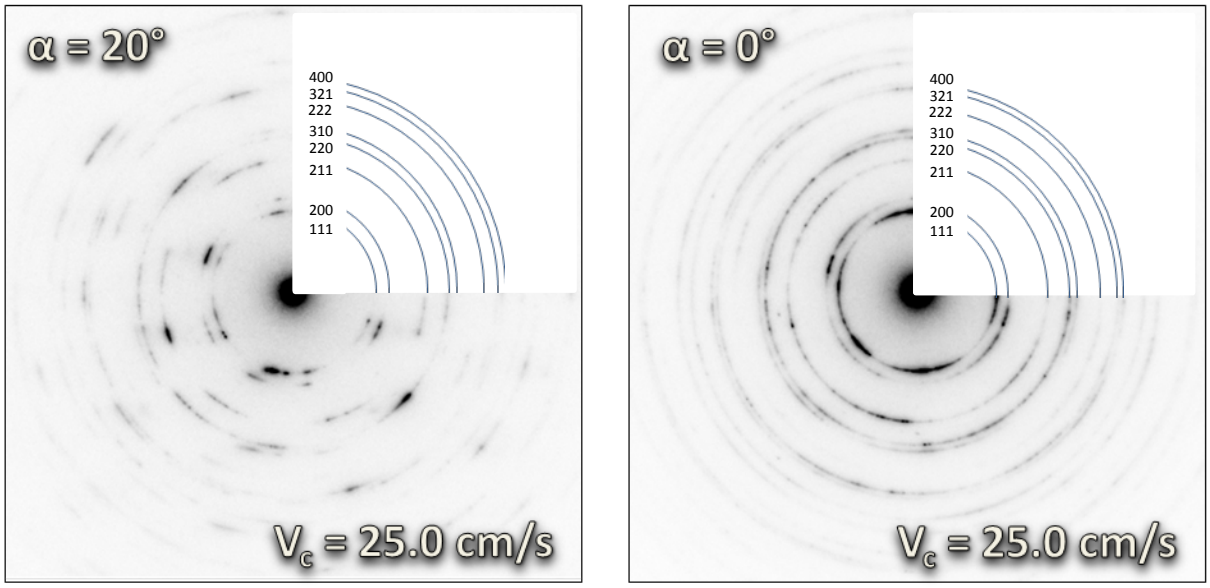

Figure 12 SAD patterns collected from the chips produced at 25.0 cm/s using the 0° and 20° raking angle tools, with indexed quarter circles representing diffraction rings corresponding to austenite FCC planes.

At the highest velocities, 25cm/s, the reduced radial broadening of the intensity maxima in the SAD patterns indicates a decrease in stored strain, which possibly is an effect of increased chip temperature during deformation. It is clear that the tool velocity, which affects both the effective strain rate and temperature during deformation, has significant effects on the scale and morphology of the resulting microstructure in the chips, while tool velocity effects on the microhardness of the chips are surprisingly minimal or essentially absent.

6.2 EFFECT OF TOOL ANGLE ON RESULTING MICROSTRUCTURE

In order to illustrate the effects of the tool angle, α, on the resulting chip microstructures, in this section specifically experimental observations and measurements obtained from chips created at the same velocity, V_c = 12.5 cm/s, with the 0° and 20° degree tool angles will be presented and discussed in some detail. These two conditions (referred to as 0° and 20° chips in this section) have been selected for additional more detailed investigation of their microstructures using TEM based OIM with the goal to elucidate the correlations between microstructure and mechanical property changes. Figure 13 shows example TEM-BF images, the associated SAD patterns of a 20° and a 0°chip microstructure, and TEM-OIM scans collected using the ASTAR™ system. This combined approach of quantitative TEM based characterization techniques makes identification of the most important microstructural differences, for instance, regarding the magnitude of the grain scale refinements, for the two different processing conditions readily apparent.

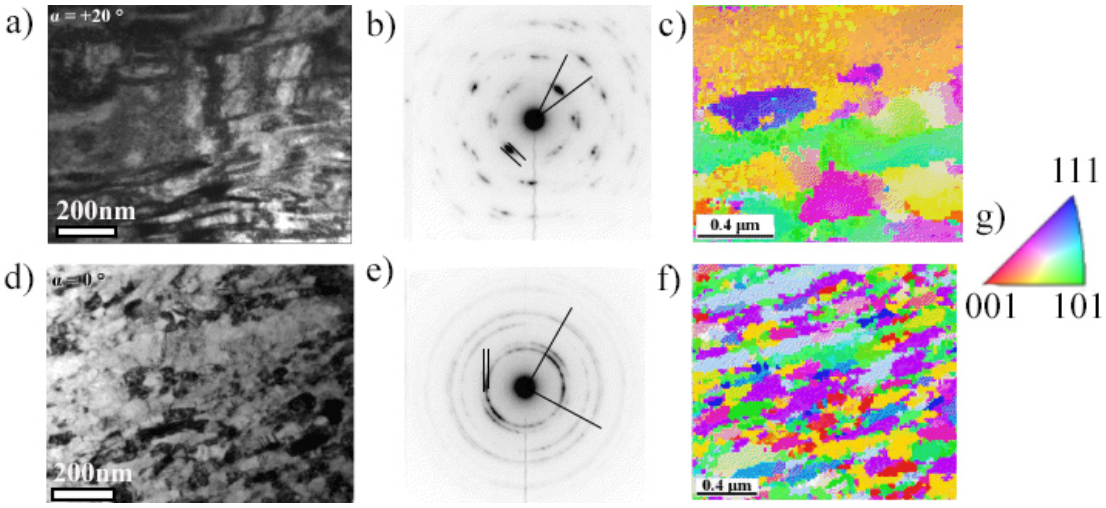

Figure 13 (a) Multi-beam BF TEM image of a 20° chip; (b) diffraction pattern (DP) including radial broadening Δk and circumferential arc markers corresponding to BF in (a); (c) IPF map of a 20° chip; (d) multi-beam BF TEM image of a 0° chip; (e) DP with Δk and arc

The diffraction contrast observed in the BF image of the 20° chip (Figure 13a) is consistent with that of a heavily cold-deformed state. The BF images obtained for the 20˚ chips consistently show a very high dislocation density and the formation of dislocation walls and a sub-grain cell structure. In the associated selected area diffraction pattern (Figure 13b), only a few maxima are observed, indicating the presence of a relatively small number of differently orientated grains in the field of view of the associated BF image. Additionally, as indicated by markers in Figure 13b, the 200 reflection g_{200} shows significant radial peak broadening, ΔK, parallel to g = 200, which would be consistent with inhomogeneous strain effects. The azimuthal broadening (or arcing) indicates an orientation spread of about 3°, due to the presence of several small volumes or sub-grain cells of similar orientation rotated slightly about the incident electron beam direction. The high concentration of stored strain renders grain size evaluation very

difficult when using conventional diffraction contrast, i.e., BF and/or DF imaging, TEM methods.

The combining influences on contrast in the BF images due to grain orientation, sub-grain misorientation, stored strain, and crystalline defects, can be difficult to distinguish making it a challenge to positively identify features like individual grains [78]. Additionally, when attempting to use dark field imaging to evaluate these heavily deformed microstructures, by observing intensities due to a specific range of diffraction vectors, the effects of stored strain and dislocations on misorientation within a grain can result in enough deviation from the diffraction condition that only small portions of individual grains can be identified [78]. These disadvantageous characteristics of conventional diffraction contrast TEM imaging limits their utility in the analysis of the microstructures observed here. As an alternative, precession electron diffraction (PED) pattern analysis based TEM–OIM has been applied to assist in the attempt to quantitatively determine grain sizes and orientations in the heavily plastically deformed microstructures [67]. This method obtains full precession electron diffraction patterns from small volumes of the sample probing with a 20nm diameter electron beam, which is then scanned over several square micrometers of the sample. The diffraction patterns are collected and indexed automatically enabling a complete 3-D orientation determination of each volume scanned and is not significantly affected in a detrimental fashion by the stored strain, allowing for a fully orientation based analysis of the grain size, grain shape and the misorientation in representative fields of view [67]. The orientation resolution in the template based orientation indexing of the PED patterns is limited to 1˚.

The TEM-OIM analysis determined misorientations of less than 5° between the sub-micron scale cells, which is consistent with dislocation sub-grain cell structures in the chip

microstructure established by plane-strain machining with the 20˚ tool (Figure 13c). Furthermore, analysis of the TEM-OIM data yielded a bimodal grain size distribution, with peaks at ~200 nm and ~1.3 μm (see Figure 14) for the 20˚ sample. Hence, it can be concluded that significant grain refinement occurred in the 20° chips, reducing the grain size from an average diameter, D, of about D ≈ 20μm prior to plastic deformation processing to the ultra-fine grained (UFG) or sub-microcrystalline range with about 0.1μm < D ≤≈1μm. Notably, these average grain sizes in excess of 0.1μm are far too large to result in significant XRD peak broadening for the austenite phase [75]. Hence, the peak broadening observed in the XRD scans for 20˚ tool angle and 12.5cm.s tool speed (see Figure 6) is attributed mostly to stored non-uniform strain, which is in good agreement with the conventional TEM imaging and diffraction data of the respective 20° chips (Figure 13b). The conventional TEM and XRD data are in good agreement with the OIM analyses (e.g. Figure 13c and f), which showed a mixture of UFG-scale (<1 μm) and microcrystalline (≥ 1 μm) grains, and strain-induced intra-granular misorientations of ~3°. The microstructure of the 20° chip exhibits characteristics of significantly elevated defect concentration and grain refinement, indicating that 20° tool angle linear plane-strain machining at 12.5cm/s facilitated severe plastic deformation (SPD).

Table 6 Summary of selected microstructural metrics and properties of 316L in as-received and the two different linear plane strain machined samples, referred to in the text of this section as the 20˚ and 0˚ samples/chip, for V_c = 12.5cm/s.

	As received	20° chip	0° chip
Martensite volume fraction (%)	0.6	2.7	2.8
Σn (n = 3,9,27) CSL number fraction	0.35	0.12	0.08
Mean grain size (nm) from OIM	22,000	200 1300	42
Average grain size (nm) (XRD-FWHM)	–	35	35
Stress (MPa); strain (XRD FWHM)	–	620; 0.003	492; 0.002
Calculated average shear strain	–	1.7	2.1
Strain rate (s^{-1}) calculated	–	6.6×10^2	8.3×10^2
Vickers microhardness (VHN)	159	442	489
Tensile strength (MPa)	515	1458	1647

Conventional TEM imaging of the 0° chips, e.g. the BF image and corresponding selected area diffraction pattern (Figure 13), revealed much smaller contrast features and lower dislocation density than for the 20° chips (e.g. Figure 13a, b). Unlike in the 20° chips, analysis of selected area diffraction patterns for the 0° chips (e.g. Figure 13e) revealed little or no radial or Δk broadening parallel to the respective diffraction vector direction. This is consistent with little or no non-uniform strain being stored in the microstructure. The more extensive azimuthal arcing observed in the selected area diffraction patterns obtained for the 0˚ chip samples, where the diffraction pattern shows almost complete rings (Figure 13e), is consistent with the presence of a larger number of small, newly formed grains separated by grain boundaries of larger misorientations present in the area sampled by the electron beam, signifying a transition from the low-angle grain boundary (LAGB) regime to the high-angle grain boundary (HAGB) regime, even nano-crystalline regime. These features signify an increase in the number of grains and the an orientation spread of the grains in the field of view probed. Using TEM–OIM, the nature of the nanometer-scale contrast features in the BF can be clearly identified as newly formed grains

separated mostly by HAGBs with misorientations larger than 15˚ (e.g. Figure 13f). The grain size distribution was determined and exhibited an average grain size of ~42 nm (Figure 14). This is in excellent agreement with the XRD data (Figure 6). Using the Scherrer formula the peak width can be related to the average size of the diffraction volume or grain size, which for the 0˚ tool angle and the 12.5cm/s tool velocity indicated an average grain size of ~35 ± 12 nm based on the peak width of the 111-peak of the austenite phase. Hence, it is reasonable to conclude that 0° angle linear plane-strain machining at 12.5cm/s leads to SPD microstructures that, presumably due to higher shear strain rates, associated also with higher effective temperature during chip formation, and strain (Table 6), experienced recovery and recrystallization, while inducing grain refinement to the nanoscale and an associated reduction of stored cold deformation strain.

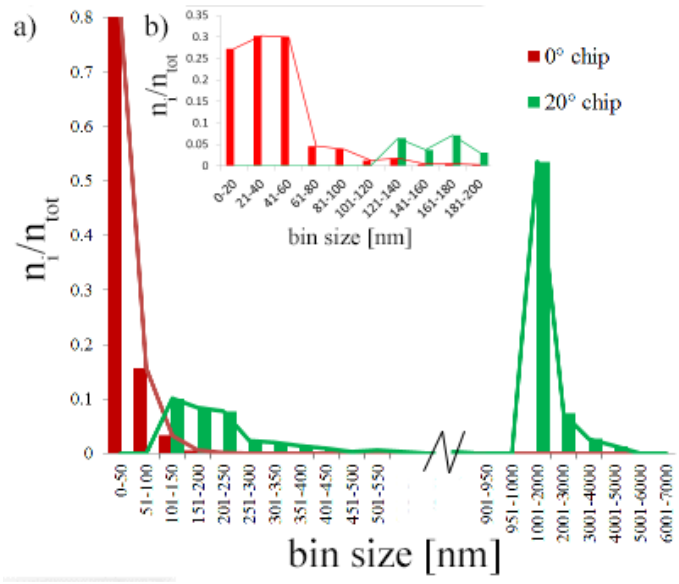

Figure 14 (a) Grain size distribution for the 20° and 0° chip samples (bin size change from 50 nm to 1 lm after 900 nm); a bimodal size distribution exists in the 20° chip. (b) Inset: refined bin size distribution for small grain sizes.

SEM and TEM based OIM methods have been used to determine grain boundary character distributions of the as-received state, and 20° and 0° chips obtained with tool velocity of 12.5cm/s for the 316L. Pertinent results are summarized in Table 6. Linear plane-strain machining leads to a significant reduction in the coincidence lattice site (CSL) Σn (n = 3, 9, 27…) boundary fraction and an increase in the fraction of general HAGBs for both processing conditions. The fraction of CSL boundaries after 0° angle tool machining is slightly lower (0.08) than after 20° angle tool machining (0.12). The TEM based OIM experimentation also enabled mapping of the spatial distributions of the secondary phase, α'-martensite phase, and has been performed for a limited set of fields of view. Such OIM based phase mapping also facilitates determination of orientation relationships between the majority matrix austenite phase and the minority secondary SIM phase and showed that most martensite grains share at least one grain boundary with the surrounding austenite that obeys either a Kurjimov–Sachs ($\{111\}_{fcc} \parallel \{110\}_{bcc}$ and $<110>_{fcc} \parallel <111>_{bcc}$) or Nishiyama–Wasserman ($\{111\}_{fcc} \parallel \{110\}_{bcc}$ and $<101>_{fcc} \parallel <001>_{bcc}$) orientation relationship (Figure 14)[27]. The orientation resolution in the template based orientation indexing of the precession electron diffraction patterns is limited to 1˚, which is too coarse to discriminate between the two different most prevalent austenite-martensite OR's (see Section 4.7.1).

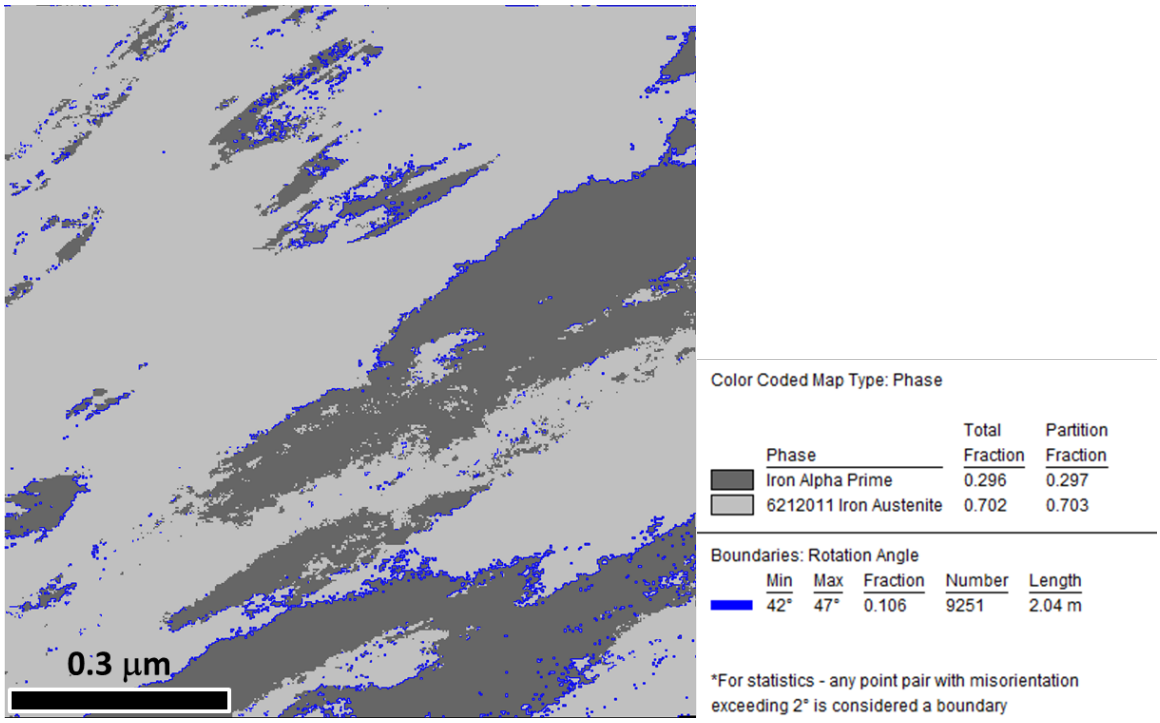

Figure 15 TEM-OIM based map, collected from a chip produced using 20° tool angle and velocity of 12.5 cm/s, showing phase fraction in gray scale and highlighting the grain boundary misorientations related to Nishiyama–Wasserman and Kurjimov–Sachs between 42° and 47° of misorientation

6.3 STRENGTHENING IN THE CHIPS

Linear plane strain machining increased the Vickers hardness of the as-received state of 159HV (corresponding to 515 MPa tensile strength) in all the chips. In the case of the two conditions studied here in depth with the use of TEM-OIM methods, namely linear raking at 12.5cm/s and with the 0˚ angle tool or the 20˚ angle tool, the strengthening mechanism could be examined more closely. The relative contributions from strain hardening and/or grain size hardening to the hardness increases of 442HV (1458 MPa tensile strength) and 489HV (1647 MPa tensile

strength) in the 20° and 0° chips obtained for V_c = 12.5 cm/s, respectively (Table 6), can be evaluated. Using a Hall–Petch constant of ~0.25 MPa $m^{1/2}$ [54, 79] and the average grain sizes determined by TEM, the contribution of the grain size strengthening to the tensile strength can be estimated. For the 20° chip the grain size reduction contribution to the increased strength is thereby estimated to be in the range of ~228–560 MPa. The large range for this estimated grain refinement strengthening effect results from the bimodal character of the grain size distribution, with maxima at ≈200nm and ≈1300nm (Table 6). For an average grain size of 200 nm the expected strength increment would be 560 MPa, while for an average grain size of 1.3 μm an increase in strength of 228 MPa would be expected. Correspondingly, for the 0° chips the Hall-Petch analysis produces an estimated strengthening from the grain size reduction to ≈40nm of ~1250 MPa. The remainder of the tensile strength, namely, ~60% (in the case of the 1.3 μm grain size) to 85% (for the 200 nm grain size) for the 20° chips and ~25% for the 0° chips, can be attributed to effects from stored strain (dislocation density), martensite phase fraction and texture contributions. The hardness measurement results are consistent with the XRD peak broadening and TEM analyses.

In summary, both of the deformation processing conditions for the linear plane-strain machining at 12.5cm/s with tool angles of 20˚ and 0˚ yield similar magnitudes of tensile strength (micro-hardness) and XRD peak broadening. However, the origins of the increased strength differ. In the case of the 20˚ chips the strengthening stems mainly from stored strain effects, while it has been attributed entirely due to a grain size refinement effect for the 0˚ chip. Importantly, in both cases the increased strength obtained in the room-temperature linear plane-strain machined 316L can be attributed mainly to combinations of grain refinement and strain storage effects, while the contribution of SIM is negligible. This is consistent with reports of

surface attrition of related austenitic stainless steels [54] and contrasts with SIM related strengthening of 316L reported after application of more conventional cold deformation processing at room temperature and at cryogenic temperatures [8].

6.4 CONCLUSIONS

316L stainless steel can be severely plastically deformed by linear plane-strain machining using 20° and 0° tool angles. XRD shows deformation texture by way of peak intensity ratio changes, grain size refinement and/or stored strain through peak broadening, and formation of strain induced α'-martensite. These XRD-based observations are consistent with microstructural changes expected from prior reports on the conventional cold deformation of 316L stainless steel. Magnetometry quantitatively identified the volume fraction of SIM (martensite) produced in the chips for each linear raking processing condition. The volume fractions of SIM present in the linear raking processed chips are significantly lower than would be expected based on results reported for 316L after conventional cold rolling processing. The low SIM volume fraction in the 316L chips implies that during the linear rake processing the temperatures experienced by the chip prevent or limit the formation of significant amounts of SIM. TEM analysis revealed significantly reduced grain scale in the microstructure of the chips, with differences being observed according to changes in processing condition. In some cases XRD peak broadening could be explained, using TEM, entirely by grain size, while in other cases TEM analysis indicated that combined effects of grain size and stored strain resulted in the increase in hardness of the chip material. Property measurement by microhardness revealed significant strengthening

in all cases. However, in contrast to more conventional cold deformation processing and other SPD processes (e.g. ECAP), the increase in strength obtained in the 316L chips obtained by linear plane-strain machining is not due to SIM (martensite) formation but is mainly a result of grain refinement and stored strain. Changes in tool angle from 20° to 0° can lead to significantly refined microstructures, and a reduction in stored strain, indicating that the chips which were subjected to higher strain rates and deformation temperatures did experience recovery and recrystallization processes. Finally, while overall strain seems to be limited to ~2.0, the strain rate, and the associated buildup of heat, imparted to the chip during the linear raking severe plastic deformation process seem to have the most significant effects on the resulting microstructures. The unique combination of large strain and high strain rate deformation accessible with linear raking results in an associated thermal excursion which facilitates nano-scale microstructural refinement and strain hardening of 316L with limited SIM formation.

6.5 FUTURE WORK

The apparent limit in strain attainable using this method prevents the investigation of potentially more extreme deformation conditions at larger total plastic strains. Developing a system design, which could constrain the chip during plane-strain machining, could lead to higher overall strains being imparted to the chip similar to the conditions found in equal channel processing for multiple passes through the ECA die. Achieving these higher strains at the high strain-rates using the straightforward process of linear raking could prove to be a useful avenue for producing significant, although relatively small in overall size, amounts of SPD strengthened stainless steel

specimens. While perhaps of limited commercial value, the realization of such extreme conditions of plastically deformed material volumes would be useful for laboratory scale studies. Future studies of additional details of the microstructure-property relationships and the effects of the extreme microstructural scale refinements on overall material response to external stimuli, e.g. from thermal, cyclic elastic straining (fatigue), thermo-mechanical and irradiation fields, would be enabled.

7.0 EFFECT OF RAKING ON SUBSTRATE

Prior reports indicated that linear raking produces a significant plastic deformation affected zone in the bulk substrate below the raking tool [14]. It is expected that the forces imparted to the surface can create a gradient of microstructures through the depth of the substrate. By exploring the scale and morphologies of the deformation microstructures present at different depths important details can be elucidated regarding how linear raking can be effectively used as a surface modification technique in 316L bulk components. Here the results of an investigation exploring how the plastic deformation processing effects on the substrate near surface regions after linear raking are presented and discussed. The microstructure of the surface and near surface region of the bulk substrate created after linear raking was analyzed by SEM, TEM, and OIM techniques, in order to gain a better understanding of how the substrate responds to the linear rake machining process. The ultimate goal of this effort is the evaluation of the potential linear raking process may have as a surface modification technique.

7.1 XRD ANALYSIS OF SUBSTRATE SURFACES

Figure 16 compares XRD scans obtained for the substrates created by plane strain machining, using two different tool-angles, $\alpha = 0°$ and $\alpha = 20°$, and tool velocities ranging from 2.5cm/s to 25cm/s, with the as-received material as a reference. Similar to the observations reported for the

chips, the substrates also exhibit changes in the relative austenite peak intensities, specifically the I_{111}/I_{200} and I_{111}/I_{220} peak ratios, indicating a deformation-induced change in texture in the near surface regions probed by the X-radiation. The XRD data is obtained from a near surface region no deeper into the substrate than on the order of about ~14μm [75]. In addition to the austenite phase, the presence of martensite phase, SIM, is also detected in the XRD scans. Analysis of the relative peak intensity, comparing the austenite (I_{111}) peaks with the martensite (I_{110}) peaks, shows the presence of martensite in all substrates except those deformed at the highest velocities (25 cm/s). Finally, all the plane-strain machining modified microstructures of the substrates exhibit similar peak broadening to that observed in the chips, attributable to either significant grain size refinement or stored strain from the plastic deformation.

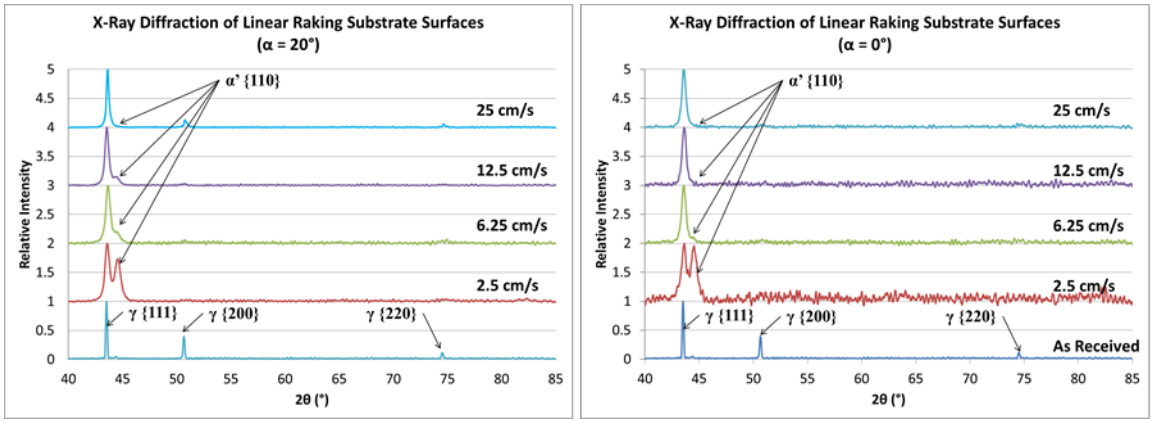

Figure 16 XRD scans of substrate surfaces creating using 2 tool angles (α) and 4 tool velocities, showing texture change through peak intensity shifts, as well as martensite volume fraction through increase in α'(I_{110}) peak intensity, and peak broadening related to stored strain or grain size refinement

Table 7 and 8 summarize the measured values for martensite (SIM) volume fraction, as determined by the relative intensity of the first austenite (I_{111}) to that of the first martensite (I_{110})

peak and the peak broadening measured in the austenite I_{111} peaks, which can be related to grain size or stored strain. Comparing these results to those observed for the chips (Section 6.1) prepared under corresponding processing conditions by linear raking, qualitatively similar trends in the evolution of the volume fraction of strain induced martensite (SIM) and peak broadening were determined. Considering the 20˚ tool angle conditions, it is apparent that the martensite content and peak broadening increased as the tool speed decreased (Table 8). For the 0˚ tool angle conditions the martensite fraction also increases for decreasing tool velocities (Table 7). However, in contrast to the 20˚ tool angle conditions, for the 0˚ tool angle conditions the effects of tool velocity on the peak broadening does not exhibit the clear inverse correlation of velocity to peak width. With the exception of the $\alpha = 0°$ and $V_c = 2.5$ cm/s combination of processing parameters, all conditions for plane strain machining show that the substrate exhibits lower or equivalent martensite volume fraction and less peak broadening than the chips obtained for equivalent plane strain machining processing parameters. However, in the single outstanding case of $\alpha = 0°$ and $V_c = 2.5$ cm/s, both the peak broadening and the martensite fraction measured by XRD in the substrate exceed the values measured in the chip, which would imply that more strain from the severe cold deformation processing is retained in the microstructures of the substrate than in that of the chip for these conditions.

Table 7 Comparison of the values measured from XRD scans taken from the substrates and chips deformed using a tool angle of α=0° scans showing the differences between calculated martensite content and measured peak broadening observed

XRD Analysis of Chips and Substrates with tool α = 0°				
Tool Velocity (cm/s)	Martensite (Vol. %)		Broadening (mrad)	
	Substrate	Chips	Substrate	Chips
2.5	23.2%	10.5%	7.62	5.48
6.25	1.5%	6.7%	4.57	6.22
12.5	1.0%	7.4%	4.31	5.18
25.0	0.3%	6.2%	3.96	5.47

Table 8 Comparison of the values measured from XRD scans taken from the substrates and chips deformed using a tool angle of α=20° scans showing the differences between calculated martensite content and measured peak broadening observed

XRD Analysis of Chips and Substrates with tool α = 20°				
Tool Velocity (cm/s)	Martensite (Vol. %)		Broadening (mrad)	
	Substrate	Chips	Substrate	Chips
2.5	20.8%	40.%	5.69	7.78
6.25	4.0%	11.0%	5.55	6.31
12.5	3.3%	2.4%	4.29	5.33
25	0.1%	1.8%	2.28	4.56

These XRD data sets clearly indicate development of deformation texture (changes in relative peak intensity), strain induced α'-martensite (SIM) transformation of the austenite, and peak broadening. This implies significant changes in the near surface microstructures of the substrates in response to the two-dimensional plane strain machining. Comparison of the XRD data sets for the chip and substrate obtained for identical plane strain machining conditions, in general indicated smaller volume fractions of SIM and peak broadening for the substrates. This

would imply that, relative to the chip, the substrate experiences a less severe thermo-mechanical exposure during the plastic deformation process. An exception to this general trend of less severe thermo-mechanical exposures for the substrates relative to the chips appears to be the case of plane strain machining for $\alpha = 0°$ and $V_c = 2.5$ cm/s, where the substrate surface appears to have been subjected to more significant cold-deformation related modification in terms of the fraction of SIM formation and strain storage than the corresponding chip.

7.2 SUBSTRATE SURFACE HARDNESS

To monitor the property changes of the substrate surfaces in response to the plane strain machining processing the microhardness values were determined using a Vickers indenter. Table 9 below shows the measured Vickers hardness for each of the eight different processing conditions for the substrates created by linear raking. As was observed in the chips (section 6.1), the hardness seems to be most affected by the tool angle. However, in contrast to the chips, these substrate hardness values are also much more correlated with the tool velocity. Thus, the hardness values are larger for the 0˚ tool angle than for the 20˚ tool angle for all velocities. Furthermore, the hardness increases with increasing tool velocity for the complete range of linear raking process conditions considered here.

Table 9 Substrate surface microhardness after linear rake machining

Tool Velocity V_c (cm/s)	$\alpha = 20°$ Hardness (VHN)	$\alpha = 0°$ Hardness (VHN)
25.0	262.7 ± 14.7	305.2 ± 19.3
12.5	280.6 ± 25.5	358.4 ± 24.8
6.25	312.0 ± 24.2	336.0 ± 24.3
2.50	325.5 ± 11.3	355.9 ± 36.7

Figure 17 illustrates the differences between chip and substrate hardness values for the 0° and 20° tool angles for the four different velocities considered here. The substrate hardness clearly shows a much more pronounced dependence on tool velocity than that of the chips. Furthermore, the substrates exhibit lower overall hardness than the corresponding chips. This would appear to be generally consistent with the comparatively reduced SIM fraction and peak broadening typically observed for the substrates relative to the chips.

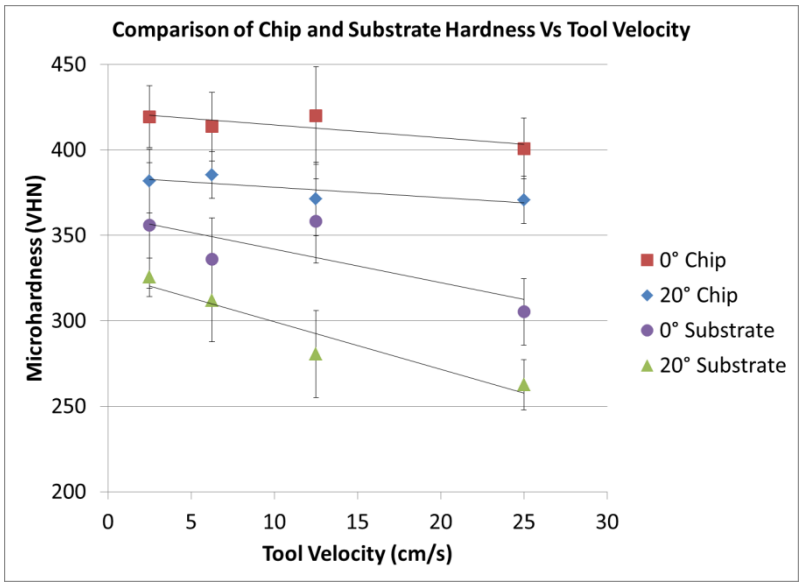

Figure 17 Chart comparing substrate surface hardness to machined chip hardness using α = 0° and 20° tool angles at 2.5, 6.25, 12.5, and 25.0 cm/s

The hardness measured in all the substrate surfaces is more than two-fold greater than the hardness measured in the bulk, indicating significant surface modification in all cases. Furthermore, by comparing the substrate surface hardness to that of the chips (Figure 17) an interesting trend can be observed. Whereas, the measured difference between substrate and chip hardness becomes smaller as the tool velocity is reduced. This would seem to imply that as the tool velocity is decreased the differences in the deformation processes and correspondingly the microstructural responses in the chip and substrate also decrease. It can be speculated that the lower rate at which the strain is imparted at the lower tool velocities allows for greater compliance of the tool with the work-piece and thereby more equivalent deformation conditions result at the substrate surface to those established in the chip.

7.3 SUBSTRATE CROSS-SECTION HARDNESS

Microhardness measurements can be a useful tool in order to determine or monitor the extent of the near surface regions that are affected by surface modification techniques [80]. Using a Vickers hardness tester and a load of 25g, profiles of hardness vs. distance from the substrate surface deeper into the bulk of the substrate were obtained. Hardness measurements were taken over cross sections of the substrates after linear rake machining in order to establish the depth dependent evolution of the microstructural and associated property changes due to the plane strain machining. Figure 18 presents the hardness vs. depth measurements obtained for $\alpha = 0°$ and 20° and a tool velocity $V_c = 12.5$ cm/s. In both cases, the substrate shows an increase in overall hardness to significant distances from the surface into the bulk material of the substrate. Significantly increased hardness values can be discerned as far as about 120 μm and about 350 μm from the substrate surface for the tool angles $\alpha = 20°$ and $\alpha = 0°$, respectively. Hence, for the 12.5cm/s tool velocity the plane strain machining modified region extends up to about to 350 μm from the surface of the substrate into the bulk.

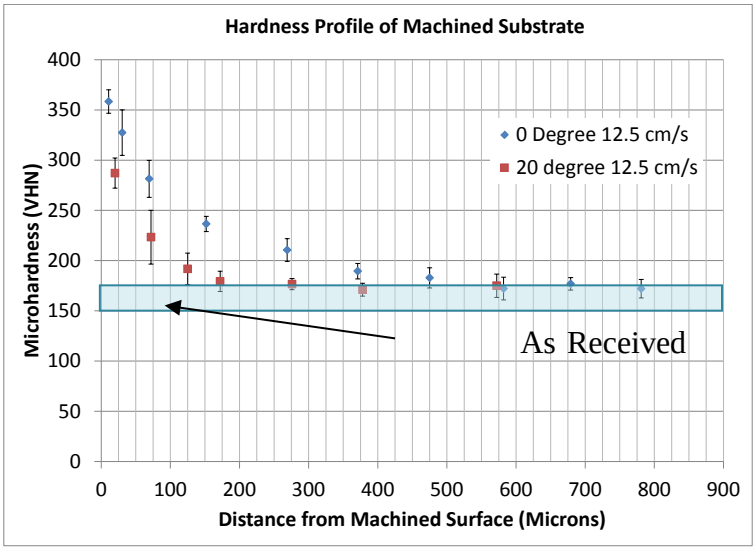

Figure 18 Substrate surface microhardness profile after linear raking using α = 0° and 20° tools at 12.5 cm/s

These hardness measurements show that the substrate surface and significant regions beyond the surface show modified mechanical properties under moderate raking conditions. Additionally, by changing the tool angle it was possible to impact the depth of the affected region dramatically, i.e., an about threefold increase from 120 μm to 350 μm by changing from the 20˚ angle tool to the 0˚ angle tool.

7.4 SEM ANALYSIS OF THE SUBSTRATE SURFACE

Using conventional secondary electron imaging (SE) in the SEM, cross sectional samples of the substrate surface were studied. The images in Figure 19 below were obtained using a JEOL JSM-5510LV in SE imaging mode and show the extent and scale of the surface modification, as well as other features of how the substrate surface is affected.

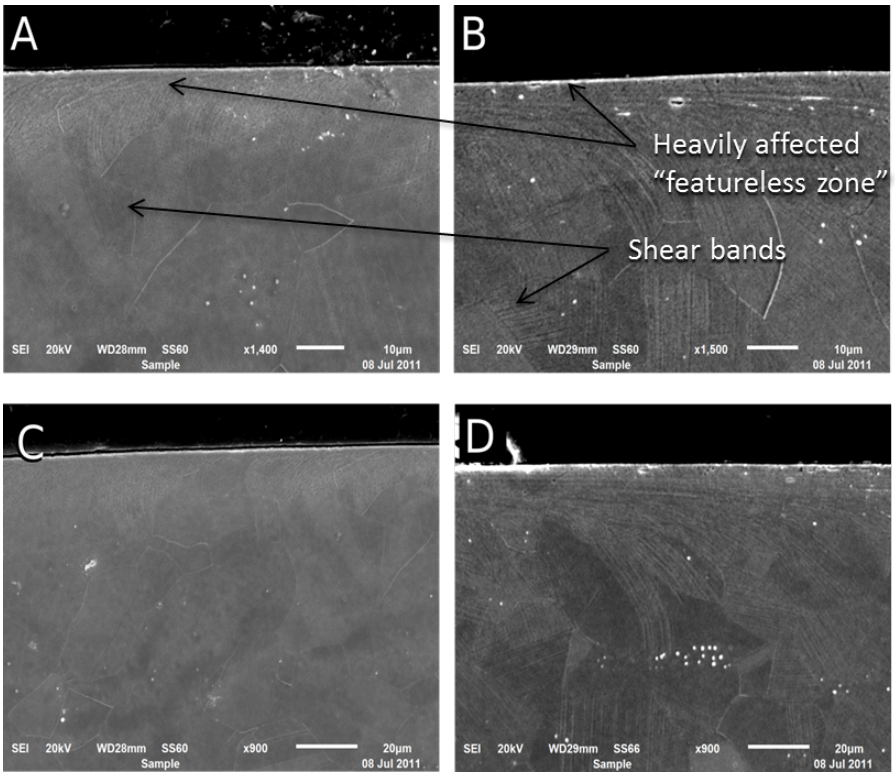

Figure 19 SE Image showing affected regions of subsurface after raking using A) 20° Tool and B) 0° Tool; Low magnification SE Image showing affected regions of subsurface post raking using C) 20° Tool and D) 0° Tool

Distinct regions, each affected differently by the raking process, can be distinguished. First, in regions near the surface where the raking has occurred, there is a highly deformed, apparently featureless zone. The micrographs in Figure 19 also show that this zone has very few identifiable grain boundaries and extends approximately 10 μm to 20 μm from the surface. Both specimens show this strongly modified near surface zone. However, nearly all other features observed in the cross-sectional microstructural studies by SEM seem to be affected differently by the linear raking parameters. While both specimens exhibit clear shear banding near the surface, the severity and direction of these shear bands is affected by the tool angle. For the sample

machined with the 20° tool, the shear bands curve slightly or mildly into the raking direction (horizontal in the figures), while in the sample machined with the 0° tool much more severe shear banding was observed. Further into the depth below the surface of the substrate, beyond this highly deformed, crystallographic featureless region, there is a region where individual grains, with a size consistent with the average grain size in the as-received state (≈ 20 μm),can be distinguished. In this latter region, most grains still exhibit significant shear banding. However, these bands seem to have a clear relationship to the crystallographic orientation of the respective grain itself rather than to the raking direction. Furthermore, this region extends much further into the substrate of the sample that has been machined using the 0° tool (starting from a depth of 10μm and terminating at about 50μm) than the equivalent region identified in the 20° tool machined sample (from 10μm to about 20μm deep). Beyond this region, the microstructure of the samples machined using the 20° tool appear to be essentially unaffected, while the microstructure of the sample machined using the 0° tool continues to exhibit some evidence of shear banding or deformation twinning penetrating as deep as 80μm below the machined surface. From these overview images it is clear that both the immediate surface and subsurface regions of the substrate are indeed modified by the raking process. Notably, the SE image based SEM analysis identifies that the plastic deformation affected microstructure in the linear raking machined substrates extends to larger depth below the substrate surface for the 0˚-angle tool than for the 20˚-angle tool processing. However, deformation affected microstructural modifications and contrast features only extend to about 80μm below the substrate surfaces while the cross-sectional microhardness measurements indicated changes in hardness to larger depth of up to about 350μm. The origins for this apparent discrepancy have not been identified here.

7.4.1 SEM-EBSD

Using SEM-EBSD scans, IPF based misorientation maps were obtained of the cross-sections of the substrate surfaces after linear raking. The OIM data sets in the figure below were obtained from EBSD scans of cross-sections of the substrate surfaces created by linear rake processing at V_c = 12.5 cm/s with tool angles of $\alpha = 20°$ and 0°. Figure 20 presents the orientation-related maps of the linear raking machined substrate surface cross-sections obtained by EBSD. In these scans different coloring represents differences in crystallographic orientation using a color-coded IPF based representation. A color legend for the crystallographic orientations in the form of a standard triangle is show as an inset. Using Image Quality (IQ), a metric determined during the automated orientation indexing using the OIM system, regions with differing indexing confidence are displayed as a grey scale image and enable identification of regions within the grains that exhibit plastic deformation induced defects, e.g., shear bands or deformation twins and perhaps even SIM patches. These OIM data based maps in Figure 19 combine crystallographic lattice orientation and local lattice strain information and therefore provide a compound representation of plastically deformed microstructures.

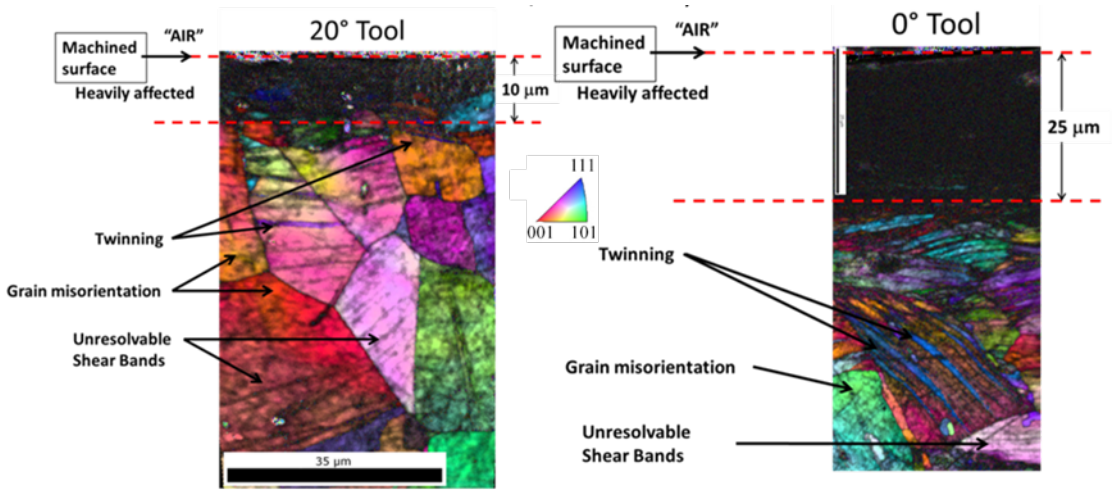

Figure 20 Cross-section SEM EBSD images showing crystallographic grain orientation in RGB and Image Quality (IQ) in greyscale of substrate surfaces after linear rake mahcining using at $\alpha = 0°$ and 20° tool angles at 12.5 cm/s

The OIM maps in Figure 20 clearly illustrate the effects of the two-dimensional plane strain machining on the microstructure of the 316L steel substrates. In both cases, for the 20˚ and the 0˚ tool angles, a region immediately adjacent to the surface subjected to linear raking exists where the EBSD patterns cannot be indexed, indicating either loss of crystalline structure or very high deformation strain induced defect content, which sufficiently strongly deteriorated the quality of the diffraction. This zone has a thickness of about ~10 µm – 25 µm directly adjacent to the surface where the linear raking was applied (labeled "Heavily affected" in Figure 20), and corresponds to the essentially featureless near surface zone observed in the SE images (Figure 19). These regions are presumably similar to the heavily deformed or severely deformed microstructures observed in the chips, where the SEM EBSD based OIM failed to produce index quality of sufficiently high value to enable definitive solution for the crystallographic phase or orientations (see Figure 9 in Section 6.1). Hence, it is reasonable to propose that there has been grain refinement (of either the austenite of the SIM phase) to the nano-scale in the heavily

affected regions identified in Figure 20, although TEM is required to confirm this observation. Beyond this heavily affected zone, grains with clear deformation twinning can be identified. Additionally, shear banding (identified through IQ metric based maps) and significant misorientation across single grains is identified in the OIM maps of Figure 20.

While similar structures can be identified in both microstructures examined here, through SE and EBSD methods, the severity of the changes and the depth below the substrate surface to which they are observed appears to depend strongly on the raking condition. The change of the tool angle from $\alpha = 20°$ to $\alpha = 0°$ significantly increased the depth of the heavily affected region and the region of twinned grains. Heavily twinned grains were identified as far as 60 μm from the surface in the $\alpha = 0°$ substrate and only to ~20 μm for the $\alpha = 20°$ substrate surface. The cross-sectional SEM data confirmed that modification to the substrate surface microstructures can be achieved using two-dimensional plane strain machining, with significant deformation defects observed in the microstructures as far as 60 μm from the substrate surface, effectively three grain size diameters of the as-received 316L. The microstructures present in the substrates show substantial amounts of stored strain energy, represented by the shear bands, deformation twins, and the heavily affected regions, which could prove important in attempts to establish more stable microstructures through subsequent thermal processing of the substrates after application of two-dimensional plane strain machining.

7.5 TEM ANALYSIS OF THE SUBSTRATE SURFACE

The regions immediately adjacent to the substrate surface were prepared for observation in the TEM. This region is important to examine with higher resolution methods because it corresponds

to the regions identified in the cross-sectional SEM studies as heavily affected, as well as the volumes probed by the Cu-Ka X-rays used for the XRD scans (Figure 16), which revealed the presence of SIM within the austenite matrix. It had been speculatively proposed that this near subsurface zone exhibited a nano-scale refinement of the grain size and presumably the formation of SIM phase (Section 7.4). In order to further evaluate this hypothesis TEM samples have been prepared from these surface regions of the linear rake machined substrates and were investigated by conventional BF and DF imaging and diffraction in the TEM. These TEM samples have been prepared by electrolytic jet-thinning from the bulk substrate side only. This resulted in thin sections suitable for the TEM studies that represent material volumes located no more than about 0.5µm below the original substrate surface, i.e., within the heavily modified zones (see Figure 20). Figure 21 displays representative TEM BF, DF, and SAD images obtained for the heavily affected zones of the substrate surfaces deformed using the 0° and 20° tool at a velocity on 12.5 cm/s. As in the case of the chips, the inherently nanoscale spatial resolution offered by TEM facilitates a more detailed and quantitative investigation of the plastic deformation modified microstructures than could be achieved by SEM.

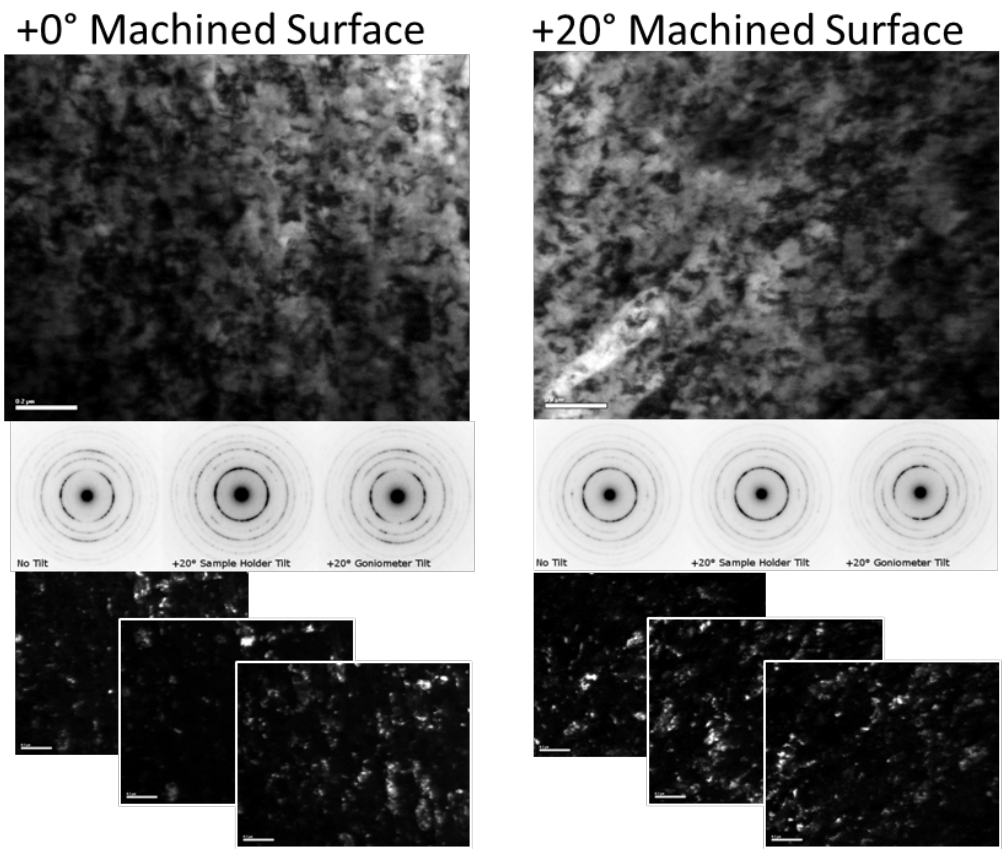

Figure 21 TEM BF, SAD patterns, and DF images of the substrate surface microstructures after linear rake machining using $\alpha = 0°$ and 20° at 12.5 cm/s

The bright field images collected show very little overall difference in the observed structures for the two different linear rake machining processing conditions. Areas with very small volumes that are oriented at different diffraction conditions, i.e., orientations relative to the incident electron beam are identified. These contrast features are consistent with those reported for highly deformed material obtained in steels and other structural alloy materials after exposure to other surface modification techniques (e.g. SMAT [60]). The associated SAD patterns collected from the same fields of view as the BF images exhibit nearly complete diffraction rings, akin to a powder pattern in a transmission XRD experiment. These nearly complete rings

of diffraction maxima are formed from large numbers of individual grains that are significantly misoriented with respect to each other and signify dramatic grain size refinement in the near surface zone after two-dimensional plane strain machining for the substrates. Additionally, SAD patterns collected at systematically different sample tilt angles identified the presence of a significant deformation texture in this region. Without the presence of a texture in the thin foil sections investigated by TEM the tilting should not have a significant effect on the distribution of intensities within each of the different diffraction rings of the respective SAD patterns. Clearly, the ± 20˚ tilts of the samples relative to the incident electron beam result in considerable and even somewhat systematic changes in the powder-like or ring-type SAD patterns relative to the un-tilted geometry, which indicates that some texturing in the probed polycrystalline aggregates. The dark field TEM images, taken with diffracted intensities from the strongest most complete diffraction rings, and from multiple beam tilts, in order to reveal grain size, show that the diffracting volumes are in the nano-scale size range. Figure 22 below shows the grain size distributions of the features identified through image analysis of numerous fields of view obtained by DF imaging. The average grain size or feature size reveled in the DF images is smaller than 100nm, $D < 100$ nm, for both linear rake machining processing conditions within the heavily affected near surface zones of the substrate surfaces.

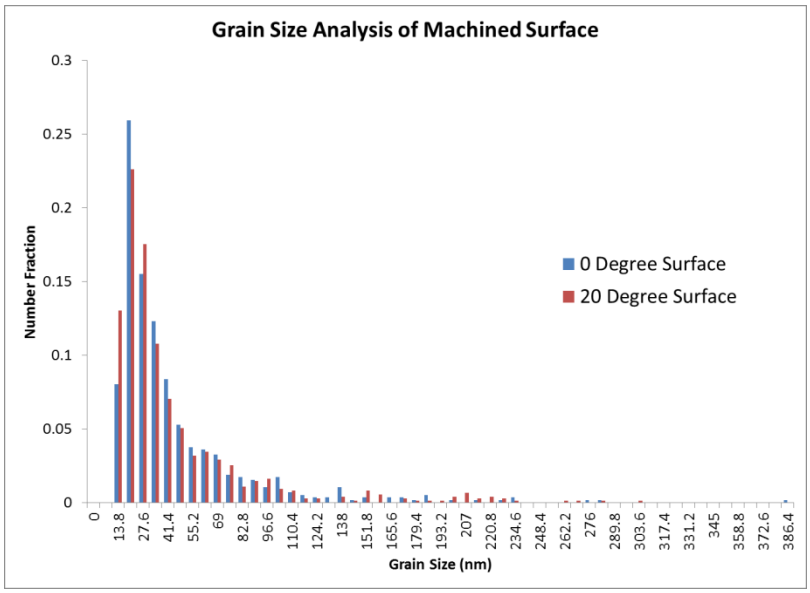

Figure 22 Results of DF image analysis from substrate surfaces machined using $\alpha = 0°$ and 20° at 12.5 cm/s

PASAD analysis, used to index the diffraction patterns, see Figure 23, revealed that in this near surface region very close to the substrate surface (~0-500 nm from the substrate-tool interface) significant amounts of α'-phase martensite can be identified. In some cases it appears that almost the entire field of view can be indexed as α'-phase martensite.

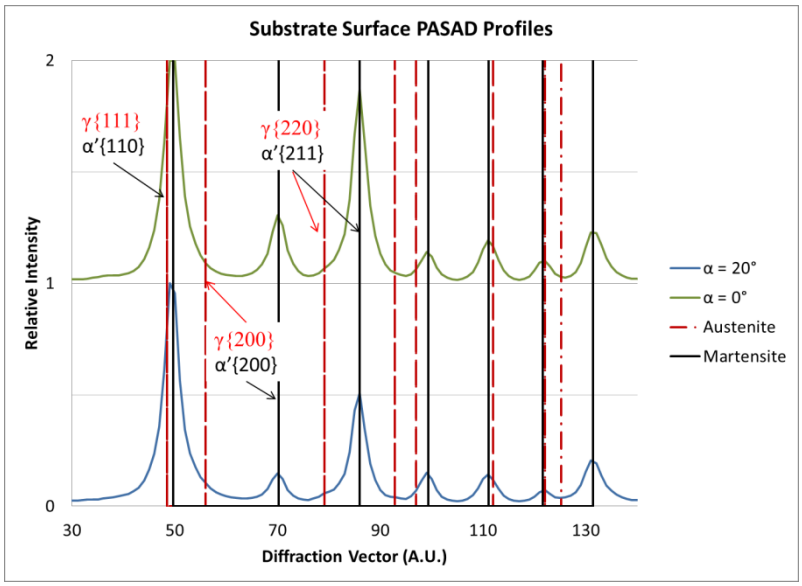

Figure 23 PASAD analysis of Substrate Surface images collected in TEM, with vertical lines used to index austenite (Red) and α'-martensite (Black) peaks**.**

These TEM results provide further confirmation of surface modification. The conditions observed here in the substrate surface near the tool interface are identified as nano-scale grains of γ- and α′-phase with a dominant fraction of α'-phase martensite. The microstructural features observed in the near surface regions are similar to those seen for other surface modification techniques. The dramatic reduction in grain size, from ~20μm prior to linear rake machining deformation processing down to about 0.03μm=~30nm after linear rake machining, suggests that severe plastic deformation of the substrate surface has occurred. The nano-scale grain refinement, α'-martensite content, and other deformation structures observed in the substrates would provide driving force for solid state reactions, e.g. reversion, recovery and recrystallization processes, within the microstructures of the substrate surface in the case of subsequent thermal processing.

7.6 CONLCUSIONS

Using a combination of microstructural examination techniques (XRD SEM and TEM, and microhardness to evaluate properties) surface modification of 316L stainless steel has been observed and quantified in this investigative effort. Through XRD, surface deformation effects have been identified; stored strain by diffraction peak broadening, changes in relative peak intensity signifying a change in texture, and finally the presence of SIM. Therefore, the XRD data provided strong evidence of surface modification after linear raking. Using microhardness, the depth of the affected regions was quantified as well as the degree to which the substrate was affected. From the heavily modified surface to the twinned grains and sub-grain misorientation identified, using both conventional SE SEM imaging, and EBSD based OIM, the microhardness depth profile could be correlated to changes in the microstructures created in the sub-surface regions. Finally, though the use of TEM, the nature and scale of the heavily affected substrate surface region was identified to be refined nanometer scale- and found to contain significant amount of SIM. The wide range of microstructures identified in the substrate as a function of depth show where recovery and recrystallization processes might be harnessed to create new and potentially high performance microstructures. These new stabilized microstructures would be achieved through a thermo-mechanical surface-modification processing route which includes 2D plane strain machining as a surface deformation technique.

7.7 FUTURE WORK

These initial results from the investigations of the substrate microstructure response to linear raking suggest that the lower raking angle of 0˚ produces a more extensive surface modification of the substrate than the 20˚-angle tool. Furthermore, this study established a facile route for future experimental evolution as a function of depth below the surface for linear raking processes substrates. This should enable correlation of property changes with microstructure for linear raking surface modified substrates. An investigation into how small changes in tool angle around 0° would affect the surface microstructure, especially regarding the depths, thicknesses or extend of the plastic deformation affected zones, could provide useful data regarding development of an understanding of how to properly design a surface processing path.

8.0 EFFECT OF HEAT TREATMENT

After application of the linear rake processing the substrate surfaces exhibited a depth dependent gradient in the level and type of microstructural modifications. Up to a depth of about 200μm – 350 μm below the external substrate surface some level of microstructural modification from the plastic deformation processing by linear rake machining could be detected in microhardness traces using substrate cross-sections. The effects from the severe thermo-mechanical processing cycle were most prominently noted in the form of a nano-scale refined zone immediately adjacent to the external substrate surface, which extended into the bulk substrate to depths of up to about 35μm for some of the linear rake machining conditions. The modified gradient microstructures contain significant defect content, e.g. SIM, nano-scale refined grains, non-equilibrium grain boundaries, deformation twins, dislocations, and therefore excess free energy that could provide driving force for potentially beneficial microstructural rearrangements and reconfigurations during subsequent thermal annealing treatments [44, 45, 53]. Thermal annealing subsequent to the linear rake machining process could result in recovery, including dislocation density reduction, reversion of SIM, changes of non-equilibrium grain boundary structures, grain growth, perhaps even recrystallization and therefore texture changes [7, 33, 53, 81]. The microstructures observed in the substrate after linear rake machining processing clearly have been driven away from equilibrium and applying subsequent annealing treatments via activation of recovery, reversion and recrystallization processes would enable creation of more stabilized

structures. Additionally, it is well understood that the cold working deformation structures observed in the substrate, including strain induced martensite, can have significantly detrimental effects on overall performance of austenitic stainless steel components, specifically corrosion and SCC related failures [44, 45]. However, attempts to revert nanocrystalline martensite microstructures, similar to those observed in the TEM of the substrate surface, to UFG scale austenite have shown great promise, by greatly increasing strength and maintaining high ductility [53]. Therefore, establishing grain scale refinement and perhaps even control of the grain boundary structures and character in the near surface regions of the modified 316L surface regions can be envisaged, but it remains to be seen whether it can be exploited in a facile manner. Notably, kinetic competition via grain growth from the large austenite grains in the regions of the substrate below the near surface regions with the linear raking modified microstructural gradient could also simply grow into the modified regions, effectively consuming these features and restoring the unmodified 316L microstructure and presumably properties of the annealed state prior to linear raking. Therefore, a preliminary investigation into effects of heat treatments was conducted using a combination of *in-situ* TEM heat treatments, as well as more conventional *ex-situ* isothermal laboratory heat treatments in an ultra-high vacuum furnace. From the previous investigations, the substrate surface microstructures immediately adjacent to the tool-work interface are very similar for both the 0° and 20° tool angles at the tool velocity of 12.5 cm/s. However, the substrate deformed using the 0° tool was chosen for the preliminary investigation of annealing treatments on the microstructural response due to the more extensive subsurface deformations extending to greater depths below the external surface.

8.1 IN-SITU HEAT TREATMENTS

Using a single-tilt TEM heating holder samples extracted from the nanoscale refined zone immediately adjacent to the external substrate surfaces have been studied in the Jeol JEM-2000FX, TEM instrument operated at 200kV. A single-tilt heating holder, model EM-SHH4, was used, with the capability to heat the TEM foil up to 1000 °C using resistive heating. This enabled direct observation of dynamic processes in response to the thermal stimulus during annealing. The TEM samples include electron transparent foil sections representative of the most severely modified volumes from no deeper than about 500 nm = 0.5μm below the external substrate surface. These in-situ heating TEM experiments allowed study of the most severely plastic deformation modified substrate surface region in isolation from the deeper less significantly modified microstructural subsurface regions of the substrate. The heat treatments applied in-situ included an isothermal exposure to 700° C for up to thirty minutes and a subsequent increment heating up to 900˚C. At the lower temperatures of 700˚C, only recovery processes are expected to occur, while reversion of SIM or recrystallization are not expected or at least limited, based on reports for annealing of conventional grain scale austenitic steels after cold work [82]. Given that the XRD data in combination with the electron microscopy observations of the substrate cross-sections (Section 7.0) indicated that the zone immediately adjacent to the rake tool modified surface comprised nano-scale SIM phase recovery assisted reversion can be expected to occur at lower temperatures and over shorter times of transformation than in much larger grain scale austenitic stainless steel[81, 83]. Hence, the 700˚C isothermal in-situ heating TEM experiments have been performed in order to monitor the stability of these refined microstructures and possible reversion of SIM at this relatively low temperature in terms of α'-martensite process reversion. Subsequent to the 30 minutes annealing at 700˚C the in situ heating stage was set to

increase the temperature to 900° C and held for 3 minutes. This enabled observation of how the microstructure evolves at temperature normally associated with recrystallization and grain growth in cold deformed austenitic stainless steels [84]. During this experiment the sample was observed continuously and images and selected area diffraction patterns have been recorded periodically to document the microstructural changes.

Figure 24 and 24 below show bright field TEM images collected after 600s (10min), 1200s (20min), and 1800s (30min) during the isothermal treatment at 700° C, along with their corresponding SAD patterns (shown in inverted contrast as 'negatives' in Figure 24) and the associated PASAD profiles (Figure 25). The PASAD profiles in Figure 25 are somewhat equivalent to powder diffraction patterns obtained by XRD diffractometer experiments in a Bragg-Brentano geometry and represent the azimuthal integration of the intensities integrated for each diffraction pattern of the respective SAD patterns. The PASAD profiles represent relative intensities for the range of diffraction angles observed in the SAD pattern[68].

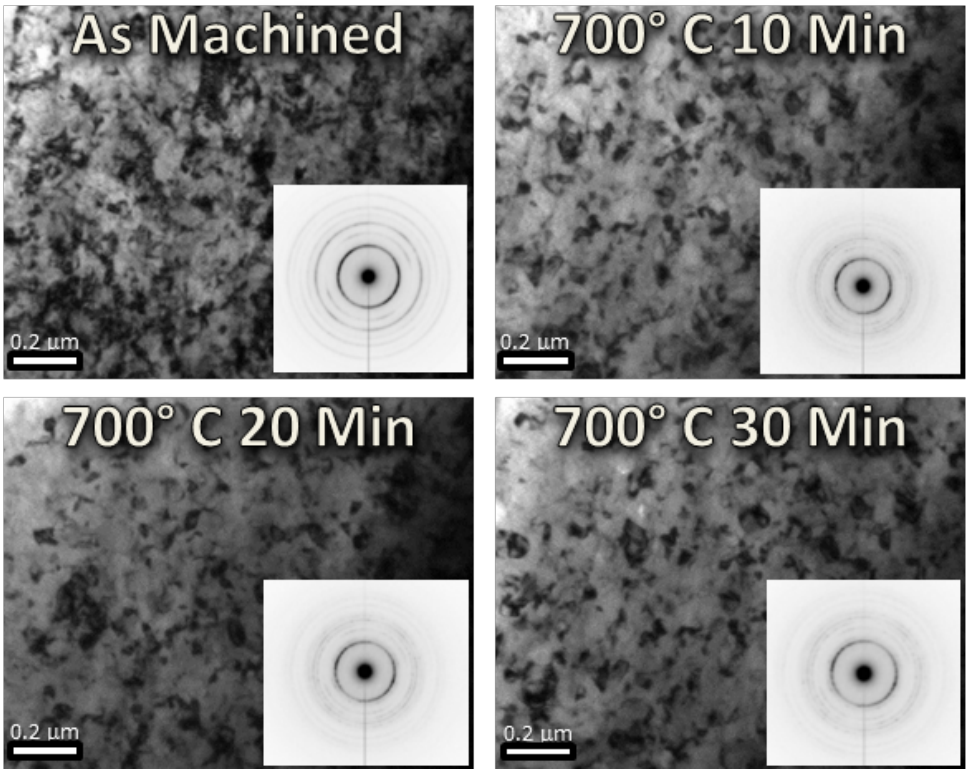

Figure 24 TEM BF and SAD patterns of substrate surface ($\alpha = 0°$ and $V_c = 12.5$ cm/s) during in-situ heat treatment at 700° C for 10, 20, and 30 minutes

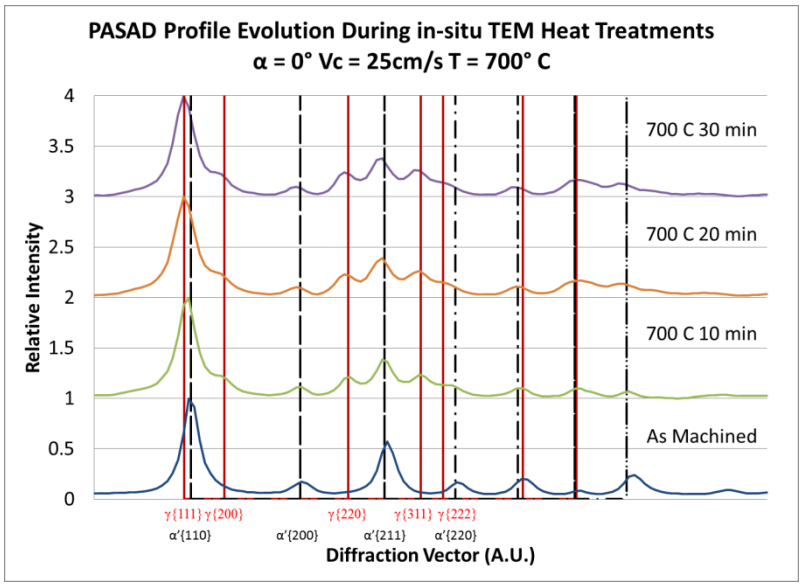

Figure 25 PASAD profiles of associated SAD patterns from Figure 24 of substrate surface ($\alpha = 0°$ and $V_c = 12.5$ cm/s) during in-situ heat treatment, with select austenite (Red) and martensite (Black) peaks indexed.

The microstructures of the substrates after linear raking were comprised of primarily nano-scale SIM grains with little to no austenite phase signal discernible in the SAD and PASAD profiles. Changes in the microstructures are qualitatively noticeable in the contrast features recorded in the BF TEM images and more quantitatively in the associated SAD and PASAD profiles obtained by post-acquisition processing of the SAD. Basically, relaxation of stored strain, reversion of SIM to austenite, and presumably some small level of grain growth occur during the 700˚C annealing over the time period of 30min (1800s). Initially, during the 700˚C in-situ TEM annealing first rapid contrast feature changes, observable changes happening on the time scale of seconds, are associated with strain relaxation, recovery assisted dislocation annihilation and presumably, very minor grain growth. However, recording images of sufficient quality at these short times after reaching the 700˚C isotherm is difficult as the heating stage

exhibited significant mechanical instability after the heating cycle, causing unacceptable image drift in the TEM. Image drift is even more significant while the temperature is changing during heating up and cooling down periods. As early as 10 minutes after reaching the 700° C isotherm, see Figure 24, the deformed structures have clearly begun recovering but grain growth appeared to be relatively limited, retaining a fine submicron- near nano-scale microstructure. After 10 min at 700˚C the SAD patterns still show relatively complete diffraction rings, prior to annealing essentially entirely associated with the SIM phase, which now include intensity from new austenite phase diffraction rings. The retention of the nearly complete ring type morphology of the SAD indicates that a nano-scale grain size is retained, i.e., a very large number of differently oriented grains are included in the field of view and contribute to the SAD. This is consistent with the qualitatively essentially unchanged contrast in the BF TEM images corresponding to the states prior to and after 10 min of annealing at 700˚C. The appearance of SAD intensity corresponding to austenite in addition to the SIM rings, perhaps more clearly illustrated the corresponding PASAD (Figure 25), signify reversion of SIM phase grains into a wide variety of new small austenite grains. The imaging and SAD data obtained after 20 and 30 minutes annealing at 700˚C still exhibit a combination of γ-austenite and α'-martensite rings, with nearly no variation compared to the state attained after 10 minutes at 700° C. Hence, it can be concluded from the isothermal annealing during the in-situ heating TEM experiments at 700°C that some recovery assisted phenomena and some reversion of SIM to austenite and minor grain growth happen very quickly, while grain growth is very limited. The SIM reversion reaction is not complete after 30 min at 700˚C and appears to be stalled during or after and not longer than about 10 min of annealing during the in-situ heating TEM experiments. This may be due to thin foil section artifacts or effects, such as surface pinning of austenite and martensite grain

boundaries by the development of surface oxides and sample contamination layers [78, 85]. In comparison to bulk 316L a dramatically nano-scale grain refined microstructure is retained in the TEM foil sections after up to 30 min annealing at 700˚C.

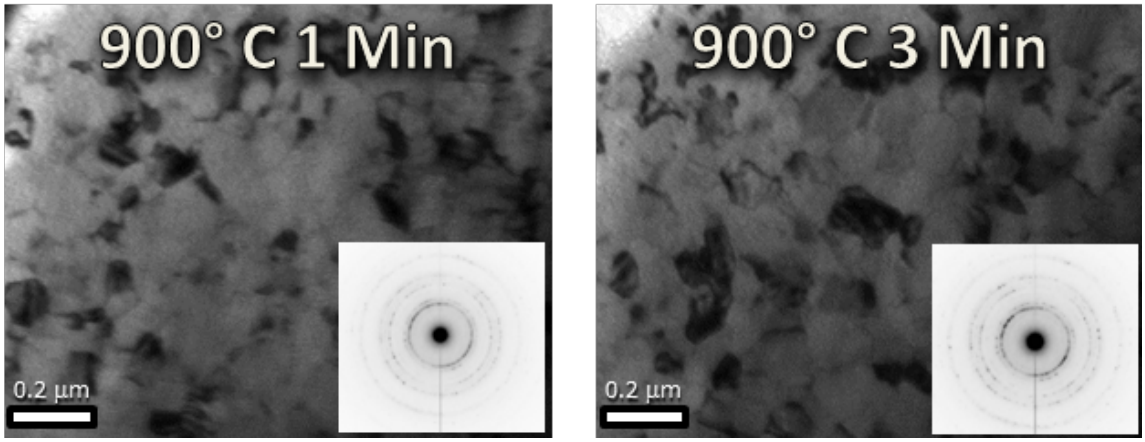

Figure 26 TEM BF and SAD patterns of substrate surface ($\alpha = 0°$ and $V_c = 12.5$ cm/s) during in-situ heat treatment at 900° C for 3 minutes after 30 minutes at 700° C

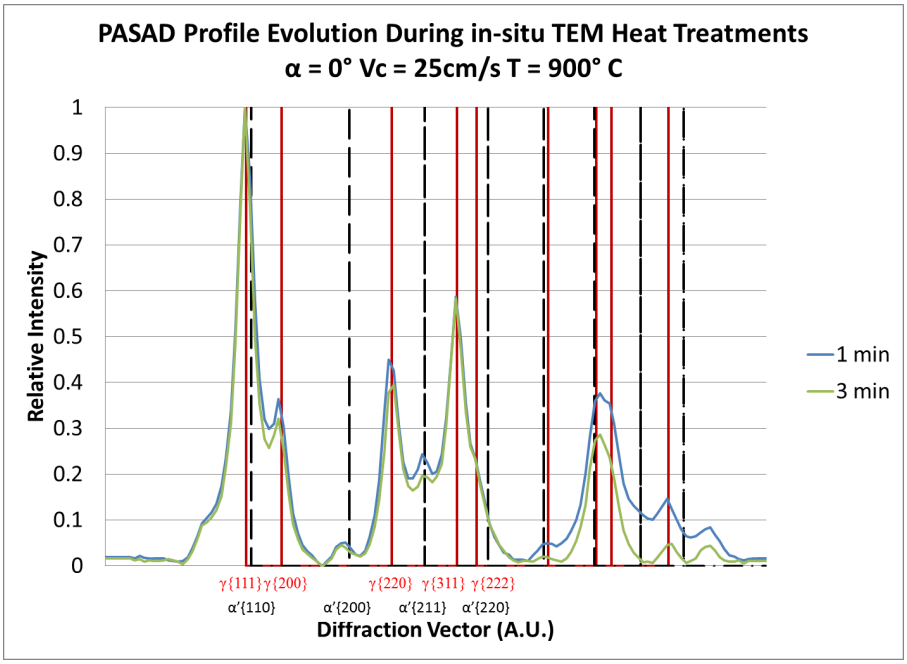

Figure 27 PASAD profiles of associated SAD patterns from Figure 26 of substrate surface (α = 0° and V_c = 12.5 cm/s) during in-situ heat, with select austenite (Red) and martensite (Black) peaks indexed.

The subsequent increase in the annealing temperature from 700˚C to 900° C resulted in significant microstructural changes. Grains that were relatively stable in size at 700° C begin to grow very quickly at the 900˚C annealing temperature. Additionally, the diffraction rings began to break up and individual diffraction spots originating from larger grains are resolvable. This signifies that the diffracting volumes have increased in size and that the area in the field of view contains significantly fewer grains with very little sub-grain misorientation than was the case prior to the 900˚C annealing exposure. The images and SAD data recorded after 3 min at 900˚C are consistent with these interpretations (Figure 26). For instance, in comparison to the BF images in Figure 24 the diffracting contrast features or grain discernible in the BF images of Figure 26 are about three to five times larger in diameter. This clearly shows that grain growth

has occurred. Analysis of PASAD profile extracted from the SAD patterns obtained after 3min at 900˚C (Figure 27) indicates a significant reduction in the relative intensities corresponding to the SIM, α'-martensite phase, relative to the state after 30min at 700˚C. However, even after 3 minutes at 900° C some SIM persists. It can be proposed speculatively that the heat treatment at 700 C created small, geometrically more stable, martensite islands, or similarly that the martensite that remains after the lower temperature annealing exposure is prevented from reverting to due surface effects like pinning [86].

8.2 UHV FURNACE HEAT TREATMENT

The in-situ heating TEM experiments clearly indicated that even at the relatively low temperature of 700° C the nano-scale refined structures observed in the most severely modified zone of the substrate quickly evolved, presumably by recovery, and recovery assiter reversion and recrystallization. In order to observe how short annealing treatments at these low temperatures affect the subsurface structures lying deeper into the substrate below this nano-scale modified zone, short heat treatments were conducted in an ultra-high vacuum furnace. This should enable an assessment of how the microstructural gradient and interactions between the differently modified zones in the subsurface structures of the linear rake machining processed 316L substrates would interact with the nano-scaled refined substrate surface microstructures observed in the in-situ heating TEM experiments. Substrate bulk samples were subjected to heat treatments at 700 or 750° C for 2 minutes. The representative SEM-EBSD OIM scans of the substrate cross sections after these two different heat treatments are shown in Figure 28 below.

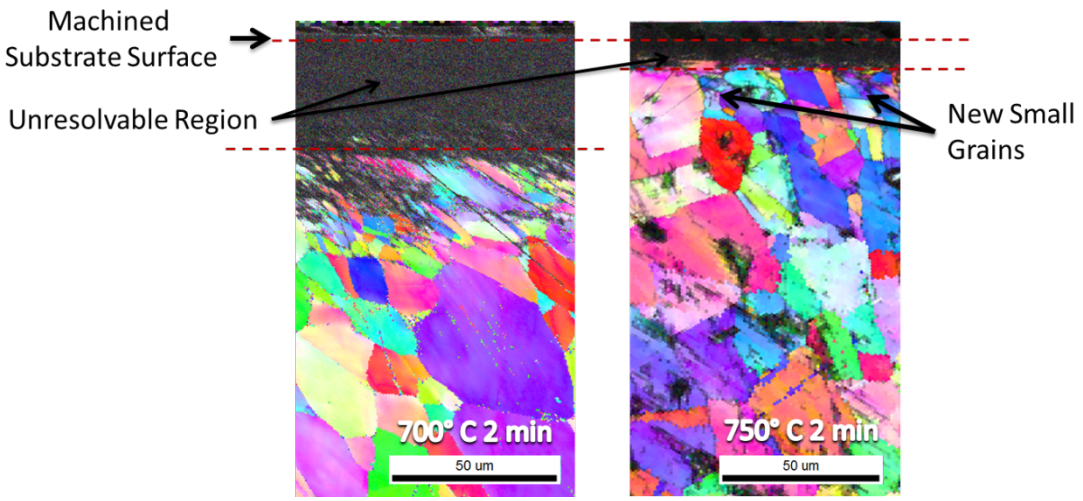

Figure 28 SEM-EBSD maps of substrate surface cross sections after heat treatments at 700° and 750° C for 2 minutes

The substrate subjected to a heat treatment at 700° C for 2 minutes shows large regions that cannot be reliably indexed, much like the heavily affected regions similar to those observed in the machined substrate in the near surface region. However, beyond these areas the deformation twins are no longer discernible in the substrate and also a reduction of other plastic strain related features (i.e. sub-grain misorientation) can be noted. These observations show that this short exposure to a relatively low temperature does result in some recovery of plastic deformation related defect structures. However, this treatment has not allowed for any extensive recovery and avoided the onset of any recrystallization or grain growth in the nano-scale refined "heavily affected" or "unresolvable regions" seen in Figure 28. In contrast, the EBSD scans collected after heat treatment at 750° C for 2 minutes show drastically different microstructural features. First, as in the initial low temperature heat treatment all of the deformation twins have disappeared. Furthermore, most of the sub-grain misorientation features disappeared.

Significantly, the “unresolvable regions” at the substrate surface have been greatly reduced in extent, and new, seemingly equilibrated grains have formed in the areas immediately adjacent to the machined surface. These new grains appear to be smaller than average grain size or the bulk as-received 316L grain size ,of approximately 20 μm. These new, smaller grains with equilibrated microstructure have very little misorientation, showing that with a small increase in temperature, for even a short heat treatments of 2 minutes at 750° C, a new surface microstructure with potentially improved properties can be created from the surface modified substrate.

8.3 CONCLUSIONS

Here a brief investigation into how heat treatment of the modified substrate microstructures can be used to create new equilibrated microstructures has been presented. Using the TEM, in-situ heat treatments showed that even brief exposures at temperatures as low as 700° C allowed for at least some reversion of SIM and recovery of the deformation structures present in the substrate surface after linear rake machining. Further investigation of how both the surface and subsurface microstructures respond to these heat treatments was then conducted using SEM-EBSD. The SEM-EBSD OIM data-sets show that new microstructures can be achieved with even short exposures to relatively low temperatures of annealing, e.g. 700-750 °C. At these low temperatures recovery of the deformation defects and limited grain growth has been observed. With these results, the viability of efforts to further explore two-dimensional plane strain machining as a possible thermo-mechanical processing route to obtain modified surface microstructures in 316L can be confirmed.

8.4 FUTURE WORK

The promise shown here by these heat treatment experiments opens possible paths to explore the recovery, recrystallization, and grain growth through systematic investigation on the effect of time and temperature on the resulting microstructures in the substrate surface. Furthermore, considerations may have to be given to how the thermal activation of the severely deformed gradient of microstructures in the substrate surface regions can be controlled during annealing in order to enable control over dissipation of the excess internal energy stored in the machined microstructures. Additionally, investigations into how annealing parameters might affect grain boundary character and other grain boundary engineering characteristics make further investigations on this matter very enticing.

9.0 DISCUSSION AND CONCLUSIONS

The two-dimensional plane strain machining process known as linear raking has been applied to 316L stainless steel and the effects of major process parameters, e.g. the cutting tool angle and the cutting velocity, on the evolution of the microstructure and mechanical properties resulting in the chip and the near-surface region of the bulk substrate have been studied. The study of the chips produced by linear rake machining allows for controlled and measurable changes of the strain and strain rates imparted during this novel, nominally room temperature, cold deformation process. Hence, study of the chips facilitates meaningful comparison with other strain paths of cold deformation processing. Therefore, establishing the effects of strain and strain rates in microstructure and property changes in the chip, due to linear rake machining, allows for a more effective evaluation of these processing parameters than only using the substrates could provide. Using tool angles of $\alpha = 0°$ and 20° at the four velocities of V_c = 2.5 cm/s , 6.25cm/s, 12.5cm/s, and 25 cm/s, a wide range of resulting large magnitudes of strain ($\gamma \approx 1.5$ to 2.3) were imparted at a range of high strain rates ($\dot{\gamma} \approx 150\ s^{-1}$ to $1700\ s^{-1}$) to the work pieces of 316L. The analysis of the actual strain and strain rate imparted to the chips during linear raking showed that the amount of deformation can easily be changed by adjusting the tool speed and angle, enabling the application of a broad spectrum of deformation conditions. The in-situ temperature measurements, obtained by use of an IR-Camera during the raking process, showed a strong dependence of the measured temperatures in the chips on the effective strain rate. Under most

linear raking conditions the maximum temperatures during the plastic deformation processing have been observed for the location at or in close proximity of the tool-chip interface, where contact friction during the orthogonal cutting related linear raking process would be expected to generate maximal adiabatic heating. However, the interesting observation of local temperature maxima for near mid-cross-section regions of the chip at locations far away from the tool-chip interface for the higher strain rate linear raking conditions would appear to be inconsistent with a sole local heat source at the tool-chip interface. The observation of these local temperature maxima in unexpected locations of the linear raking processed chips for the high strain rate conditions would be consistent with local exothermic solid-state reactions occurring shortly after the plastic deformation process occurs in the shear zone of the chips, which has been proposed speculatively. The solid-state reactions, e.g. martensite reversion, occurring during the high strain rate linear raking processing would also be consistent with the reduced volume fractions of martensite that have been observed for these conditions by VSM and XRD.

Microstructural analysis and property measurements of the chips produced by linear raking have been performed using a multi-scale approach, including XRD, VSM based magnetometry, Vickers microhardness, SEM, SEM-EBSD-OIM, TEM, and TEM-OIM. This facilitated a systematic investigation on the influence of the processing parameters (α, a_0, V_c) and the corresponding strain, strain rates, plastic deformation related temperature changes, on microstructure development in the chips. The microstructural changes observed in the chip, from deformation texture, α'-martensite (SIM) formation, sub-grain misorientation and grain size refinement, showed that the chips produced through linear raking of 316L exhibit significant strengthening and grain refinement through severe plastic deformation behavior, while avoiding significant SIM formation. It was also observed that the presence of dynamic recovery and

recrystallization processes depended on the raking parameters. This correlates with the IR-thermography measurements, which would appear to be indicative or at least consistent with occurrence of recovery and recrystallization, and SIM reversion related processes during the thermomechanical cycle associated with linear rake processing and chip formation. Due to the significant temperature increase observed as strain rate is increased the solid-state reactions are enabled and yield enormously grain size refined microstructures. While the thermally activated processes are enabled by the temperature increase associated with the linear raking process they may actually not occur simultaneously with the plastic shearing in the process zone of the 316L specimens but rather subsequently while the chip material is cooling down. Hence, these are not considered to be dynamic solid-state reactions, as they do not appear to occur simultaneously with the plastic straining processes of linear raking. Under certain linear raking process conditions nanoscale refined, nearly all austenite phase microstructures, with an average grain size ≈40nm, and SIM fraction ≈2 vol%, have been established in the chips. These nano-scale refined austenite microstrucures exhibited considerably increased mechanical strength, on the order of 1.6 GPa. The microstructure of the 316L prior to linear raking consisted of approximately 20μm grains and up to 0.5 vol% ferromagnetic phase, with mechanical stranth on the order of 0.5 GPa. The prevention or limitation of the SIM formation during the linear raking process for the chips has been attributed to the significantly increased temperatures (up to ≈ 400K or ≈ 126˚C, as measured for the chips) associated with the large strain rates (up to about 1700 s^{-1}) that have been applied. Notably, the start temperature at which significant α'-martensite is expected to form after plastic deformation under more conventional cold deformation processing conditions, $M_{d(30/50)}$, for 316L is estimated to be T ≈ -33° C, which is significantly below the temperatures experienced by the material of the chip. Hence, in contrast to the

expectation based on the more conventional cold deformation processing of 316L, the small but significant martensite fractions present in the linear raking prepared chips shows that the extreme deformation strains, even at the locally elevated temperatures higher than the $M_{d(30/50)} \approx -33°$ C, are sufficient to trigger the SIM transformation observed here. This might imply that the empirically determined $M_{d(30/50)}$ temperature can be affected significantly by the details of the plastic deformation path, which deviate substantially from processing parameters typical of conventional cold deformation processing. The unusual combination of large strain and high strain rates obtained in linear raking produces a different microstructure response than would be predicted from empirical knowledge based on cold working by conventional cold rolling type processing. Moreover, the strains measured in the chips clearly showed a saturation level of about $\gamma \approx 2.2$ to 2.3 for the amount of strain the linear raking process can impart to the 316L chips. This provides evidence that tool/work-piece compliance is an issue and developing a method to constrain the chips being produced may allow for greater strains and strain rates to be imparted to 316L using the linear raking based plastic deformation process.

Investigations of the raked substrate surface have been performed in order to explore the potential of linear raking as a surface modification technique. Through XRD and TEM, the immediate substrate-tool interface was found to exhibit a heavily affected substrate surface region, which displayed strongly scale refined nano-scale features, as well as significant SIM content. This indicates that SPD is also achieved in the substrate surface, but without the very effective suppression of SIM formation that was observed in the chips. This would be consistent with arguments considering the thermal cycles resulting in the chip versus in the near surface region by the bulk substrate. The limited ability to dissipate the process heat generated in the vicinity of the tool-chip interface for the case of the chip results in significant temperature

excursions well above the ambient temperature of ≈ 300K, thereby reducing the tendency of SIM formation in the 316L. SIM formation in the 316L chips may have been reduced further by dynamic solid-state reactions such as dynamic reversion of SIM in the plastic process zone. While these dynamic processes are difficult to prove directly, it is clear that the chip volumes experience a thermal exposure of about 100 K to 150 K due to the process heat from linear raking. Conversely, the continuity of the linear raking process affected and locally heated zones near surface regions of the substrate with the essentially unaffected material volumes of the bulk underneath, further away from the machined surface, enables facile transport of the frictional heat from the vicinity of the cutting tool. The temperature excursion experienced in the substrate, even the near surface region most significantly affected by the linear raking induced plastic deformation processes, are much smaller than for the corresponding chip material, resulting in more significant SIM volume fractions under the large strains imparted. Investigations of the sub-surface regions using SEM-SE and EBSD methods identified considerable volumes with new deformation affected structures at significant distances (up to 60 μm) from the substrate surface. The microhardness depth profile correlated strengthening in these regions to changes in the microstructures created in the sub-surface regions. Microhardness measurements indicated increased values to even greater depth below the surface, e.g. up to ≈ 350 μm. The gradient of microstructural morphologies and microstructural features identified in the substrate surface and sub-surface regions show that linear raking is indeed capable of producing surface modified microstructures in 316L. However, these plastic deformation modified structures were limited to depths equivalent to two up to about four, original 20μm diameter, grain sizes. Also, the limited SIM formation observed in the chips was not observed in the substrate surface. This is most likely due to significantly lower temperatures observed in the substrate during the raking process,

allowing for martensite to form more readily in the 316L. Finally, it was shown here that some control over the extent of substrate that can be affected through linear raking is possible by changing the raking angle. Therefore, more significant surface modification would appear to be possible through the use of more severe (more negative) raking angle tools. In this way, it might to possible to achieve microstructures more similar to those observed in the chips, i.e., including austenitic grains with nanoscale size, by increasing strain imparted to and temperatures experienced by the substrate surface. This speculative proposition relies on the assumption that the processes, such as reversion of SIM, can be activated as a part of the plastic deformation process in the substrate of the linear raking process affected near surface regions of the bulk 316L substrate.

In order to explore the feasibly of using the surface modified structures identified in the 316L substrate, a variety of preliminary annealing experiments were performed on substrate surface specimens. Initial in-situ TEM heat treatments showed that even brief exposures at temperatures as low as 700° C allowed for at least some reversion of SIM and recovery of the deformation structures present in the substrate surface after linear rake machining. Ex-situ heat-treated samples analyzed using SEM-EBSD demonstrated that areas of newly formed relatively strain free grains of austenite could be identified, even after short exposures to relatively low temperatures, e.g. 700˚C and 750˚C, for relatively short times, e.g. 180s. Here the viability of two-dimensional plane strain machining as a possible thermo-mechanical processing was examined and might be thought of as promising. It would seem that some control over the scale of the final microstructures of the substrate surface and sub-surface regions could be achieved through appropriate combination of time and temperature during annealing treatments. Through such post-deformation annealing treatments it might be possible to create microstructures in the

near surface regions of the substrate modified by linear raking that exhibit significantly improved resistance to degradation, e.g. by prolonging the incubation times typically preceding significant initiation of failures, like those observed in 316L in commercial nuclear power plants for IASCC.

In conclusion, an extensive exploration of the mechanical response of 316L to linear rake machining was completed. First, using the chips a wide variety of strain and strain rates were applied and the resulting microstructures correlated to combinations of severe plastic deformation processes, and in “dynamic” recovery processes. Through the evaluation of these structures substantial strengthening was realized through both stored strain as well as grain refinement, while avoiding significant SIM formation. Using the chips produced by the linear raking it has been shown that both the tool angle and the tool velocity have significant effects on the actual strain and the actual strain rates experienced by the 316L material volumes during the plastic deformation process. Also, from the identification of SPD structures and substantial SIM content in the substrate surface, as well as significantly modified structures in the sub-surface, linear raking was shown to be a potentially effective surface modification technique. Finally, the structures identified in the substrate were shown to have the capacity of forming new stabilized and relatively strain free microstructures through thermal annealing subsequent to the extreme thermomechanical processing exposures from linear raking. Linear raking has been demonstrated to be an effective and versatile method for production of severely plastically deformed and modified 316L stainless steel, with a clear set of relationships between the parameters of the linear raking method and the resulting microstructures and properties.

BIBLIOGRAPHY

[1] *World Energy Outlook 2012 Executive Summary*, 2012, International Energy Agency: Paris, France.

[2] *Status and Outlook for Nuclear Energy in the United States*, 2013, Nuclear Energy Insitute: Washington DC.

[3] *Nuclear Power in the USA*. 2013 April 2013 [cited 2013; Available from: http://www.world-nuclear.org/info/Country-Profiles/Countries-T-Z/USA--Nuclear-Power/.

[4] Allen, T., et al., *Materials challenges for nuclear systems.* Materials Today, 2010. **13**(12): p. 14-23.

[5] Was, G.S., *Fundamentals of Radiation Materials Science: Metals and Alloys*. 2007: Springer.

[6] Lamarsh, J.R., *Introduction to nuclear engineering*. 1975: Addison-Wesley Pub. Co.

[7] Shimada, M., et al., *Optimization of grain boundary character distribution for intergranular corrosion resistant 304 stainless steel by twin-induced grain boundary engineering.* Acta Materialia, 2002. **50**(9): p. 2331-2341.

[8] Eskandari, M., A. Najafizadeh, and A. Kermanpur, *Effect of strain-induced martensite on the formation of nanocrystalline 316L stainless steel after cold rolling and annealing.* Materials Science and Engineering A, 2009. **519**(1-2): p. 46-50.

[9] Prevéy, P.S. and J.T. Cammett, *The influence of surface enhancement by low plasticity burnishing on the corrosion fatigue performance of AA7075-T6.* International Journal of Fatigue, 2004. **26**(9): p. 975-982.

[10] Lo, K.H., C.H. Shek, and J.K.L. Lai, *Recent developments in stainless steels.* Materials Science and Engineering R: Reports, 2009. **65**(4-6): p. 39-104.

[11] Bruemmer, S.M., *Grain boundary composition and effects on environmental degradation*, 1999. p. 75-82.

[12] Edwards, D.J., et al., *Influence of irradiation temperature and dose gradients on the microstructural evolution in neutron-irradiated 316SS.* Journal of Nuclear Materials, 2003. **317**(1): p. 32-45.

[13] Swaminathan, S., et al., *Severe plastic deformation (SPD) and nanostructured materials by machining.* Journal of Materials Science, 2007. **42**(5): p. 1529-1541.

[14] Ravi Shankar, M., et al., *Severe plastic deformation of difficult-to-deform materials at near-ambient temperature.* Metallurgical and Materials Transactions A: Physical Metallurgy and Materials Science, 2007. **38 A**(9): p. 1899-1905.

[15] Lucas, G.E., *The evolution of mechanical property change in irradiated austenitic stainless steels.* Journal of Nuclear Materials, 1993. **206**(2-3): p. 287-305.

[16] Simonen, E.P. and S.M. Bruemmer, *Radiation effects on environmental cracking of stainless steels.* JOM, 1998. **50**(12): p. 52-55.

[17] Etienne, A., et al., *Dislocation loop evolution under ion irradiation in austenitic stainless steels.* Journal of Nuclear Materials, 2010. **400**(1): p. 56-63.

[18] Dieter, G.E., *Mechanical metallurgy*. 1976: McGraw-Hill.

[19] Meyers, M.A., A. Mishra, and D.J. Benson, *Mechanical properties of nanocrystalline materials.* Progress in Materials Science, 2006. **51**(4): p. 427-556.

[20] Jivkov, A.P., N.P.C. Stevens, and T.J. Marrow, *Mesoscale mechanical model for intergranular stress corrosion cracking and implications for microstructure engineering.* Journal of Pressure Vessel Technology, Transactions of the ASME, 2008. **130**(3): p. 0314021-0314027.

[21] Jivkov, A.P., N.P.C. Stevens, and T.J. Marrow, *A two-dimensional mesoscale model for intergranular stress corrosion crack propagation.* Acta Materialia, 2006. **54**(13): p. 3493-3501.

[22] Rose, M., A.G. Balogh, and H. Hahn, *Instability of irradiation induced defects in nanostructured materials.* Nuclear Instruments and Methods in Physics Research, Section B: Beam Interactions with Materials and Atoms, 1997. **127-128**: p. 119-122.

[23] Nita, N., R. Schaeublin, and M. Victoria, *Impact of irradiation on the microstructure of nanocrystalline materials.* Journal of Nuclear Materials, 2004. **329-333**(1-3 PART B): p. 953-957.

[24] Radiguet, B., et al., *Irradiation behavior of nanostructured 316 austenitic stainless steel.* Journal of Materials Science, 2008. **43**(23-24): p. 7338-7343.

[25] Aust, K.T., *Grain boundary engineering.* Canadian Metallurgical Quarterly, 1994. **33**(4): p. 265-274.

[26] Randle, V., M. Coleman, and M. Waterton, *The role of ∑9 boundaries in grain boundary engineering.* Metallurgical and Materials Transactions A: Physical Metallurgy and Materials Science, 2011. **42**(3): p. 582-586.

[27] Hill, R.E.R. and R. Abbaschian, *Physical metallurgy principles*. 1992: PWS-Kent Publishing Company.

[28] Palumbo, G., et al., *Grain boundary design and control for intergranular stress-corrosion resistance.* Scripta Metallurgica et Materiala, 1991. **25**(8): p. 1775-1780.

[29] Hasson, G.C. and C. Goux, *Interfacial energies of tilt boundaries in aluminium. Experimental and theoretical determination.* Scripta Metallurgica, 1971. **5**(10): p. 889-894.

[30] Sahlaoui, H., et al., *Effects of ageing conditions on the precipitates evolution, chromium depletion and intergranular corrosion susceptibility of AISI 316L: Experimental and modeling results.* Materials Science and Engineering A, 2004. **372**(1-2): p. 98-108.

[31] Jin, W., et al., *Improvement of intergranular stress corrosion crack susceptibility of austenite stainless steel through grain boundary engineering.* Journal of Materials Science and Technology, 2007. **23**(6): p. 785-789.

[32] Zhou, C.L., et al., *Effects of the cold-rolled reduction on the mechanical properties of 304 austenitic stainless steel sheets.* Kang T'ieh/Iron and Steel, 2012. **47**(10): p. 70-75.

[33] Hedayati, A., et al., *The effect of cold rolling regime on microstructure and mechanical properties of AISI 304L stainless steel.* Journal of Materials Processing Technology, 2010. **210**(8): p. 1017-1022.

[34] Spencer, K.K., et al., *The strain induced martensite transformation in austenitic stainless steels Part 1 - Influence of temperature and strain history.* Materials Science and Technology, 2009. **25**(1): p. 7-17.

[35] Talonen, J., et al., *Effect of strain rate on the strain-induced γ, → α′-martensite transformation and mechanical properties of austenitic stainless steels.* Metallurgical and Materials Transactions A: Physical Metallurgy and Materials Science, 2005. **36 A**(2): p. 421-432.

[36] Angel, T., *Formation of Martensite in Austenitic Stainless Steels - Effects of Deformation, Temperature, and Composition.* Journal of the Iron and Steel Institute, 1954. **177**(1): p. 165-&.

[37] Altenberger, I., et al., *Cyclic deformation and near surface microstructures of shot peened or deep rolled austenitic stainless steel AISI 304.* Materials Science and Engineering A, 1999. **264**(1-2): p. 1-16.

[38] de Abreu, H.F.G., et al., *Deformation induced martensite in an AISI 301LN stainless steel: Characterization and influence on pitting corrosion resistance.* Materials Research, 2007. **10**(4): p. 359-366.

[39] Mangonon, P. and G. Thomas, *The martensite phases in 304 stainless steel.* Metallurgical Transactions, 1970. **1**(6): p. 1577-1586.

[40] Breedis, J.F. and L. Kaufman, *The formation of Hcp and Bcc phases in austenitic iron alloys.* Metallurgical Transactions, 1971. **2**(9): p. 2359-2371.

[41] Schramm, R.E. and R.P. Reed, *Stacking fault energies of seven commercial austenitic stainless steels.* Metallurgical Transactions A, 1975. **6**(7): p. 1345-1351.

[42] Padilha, A.F. and P.R. Rios, *Decomposition of austenite in austenitic stainless steels.* ISIJ International, 2002. **42**(4): p. 325-337.

[43] Solomon, N. and I. Solomon, *Deformation induced martensite in AISI 316 stainless steel.* Revista de Metalurgia (Madrid), 2010. **46**(2): p. 121-128.

[44] Kuniya, J., I. Masaoka, and R. Sasaki, *EFFECT OF COLD WORK ON THE STRESS CORROSION CRACKING OF NONSENSITIZED AISI 304 STAINLESS STEEL IN HIGH-TEMPERATURE OXYGENATED WATER.* Corrosion, 1988. **44**(1): p. 21-28.

[45] Nakajima, M., Y. Uematsu, and M. Akita, *Effect of strain-induced martensite transformation on fatigue behavior of prestrained type 304 austenitic stainless steel.* Nihon Kikai Gakkai Ronbunshu, A Hen/Transactions of the Japan Society of Mechanical Engineers, Part A, 2009. **75**(759): p. 1591-1597.

[46] Smirnova, N.A., et al., *Evolution of the Structure of FCC Single Crystals upon Large Plastic Deformations.* Fiz. Met. Metalloved., 1986. **61**(6): p. 1170-1177.

[47] Languillaume, J., et al., *Microstructures and hardness of ultrafine-grained Ni3Al.* Acta Metallurgica Et Materialia, 1993. **41**(10): p. 2953-2962.

[48] Islamgaliev, R.K., et al., *The nanocrystalline structure formation in germanium subjected to severe plastic deformation.* Nanostructured Materials, 1994. **4**(4): p. 387-395.

[49] Valiev, R.Z., N.A. Krasilnikov, and N.K. Tsenev, *Plastic deformation of alloys with submicron-grained structure.* Materials Science and Engineering A, 1991. **137**(C): p. 35-40.

[50] Valiev, R.Z., Tsenev, N.K. *Hot deformation of aluminum alloys: proceedings of a symposium by the Non-Ferrous Metals Committee of the Minerals, Metals and Materials Society, Detroit, Michigan, October 8-10, 1990*. 1991. TMS.

[51] Litovchenko, I.Y., et al., *Direct and reverse martensitic transformation and formation of nanostructured states during severe plastic deformation of metastable austenitic stainless steel.* Reviews on Advanced Materials Science, 2012. **31**(1): p. 47-53.

[52] Tomimura, K., et al., *Optimal Chemical Composition in Fe-Cr-Ni Alloys for Ultra Grain Refining by Reversion from Deformation Induced Martensite.* ISIJ International, 1991. **31**(7): p. 721-727.

[53] Forouzan, F., et al., *Production of nano/submicron grained AISI 304L stainless steel through the martensite reversion process.* Materials Science and Engineering: A, 2010. **527**(27–28): p. 7334-7339.

[54] Chen, X.H., et al., *Tensile properties of a nanocrystalline 316L austenitic stainless steel.* Scripta Materialia, 2005. **52**(10): p. 1039-1044.

[55] Ueno, H., et al., *Nanostructurization assisted by twinning during equal channel angular pressing of metastable 316L stainless steel.* Journal of Materials Science, 2011. **46**(12): p. 4276-4283.

[56] Valiev, R., *Nanostructuring of metals by severe plastic deformation for advanced properties.* Nature Materials, 2004. **3**(8): p. 511-516.

[57] Valiev, R.Z., A.V. Korznikov, and R.R. Mulyukov, *Structure and properties of ultrafine-grained materials produced by severe plastic deformation.* Materials Science and Engineering A, 1993. **168**(2): p. 141-148.

[58] Lu, K. and J. Lu, *Surface nanocrystallization (SNC) of metallic materials-presentation of the concept behind a new approach.* Journal of Materials Science and Technology, 1999. **15**(3): p. 193-197.

[59] Tao, N.R., et al., *Surface nanocrystallization of iron induced by ultrasonic shot peening.* Nanostructured Materials, 1999. **11**(4): p. 433-440.

[60] Tao, N.R., et al., *An investigation of surface nanocrystallization mechanism in Fe induced by surface mechanical attrition treatment.* Acta Materialia, 2002. **50**(18): p. 4603-4616.

[61] Montross, C.S., et al., *Laser shock processing and its effects on microstructure and properties of metal alloys: A review.* International Journal of Fatigue, 2002. **24**(10): p. 1021-1036.

[62] Chivers, T.C. and S.C. Gordelier, *Fretting fatigue palliatives: Some comparative experiments.* Wear, 1984. **96**(2): p. 153-175.

[63] Arifvianto, B., et al., *Effect of surface mechanical attrition treatment (SMAT) on microhardness, surface roughness and wettability of AISI 316L.* Materials Chemistry and Physics, 2011. **125**(3): p. 418-426.

[64] Merchant, M.E., *Mechanics of the metal cutting process. I. Orthogonal cutting and a type 2 chip.* Journal of Applied Physics, 1945. **16**(5): p. 267-275.

[65] Shaw, M.C., *Metal cutting principles*. 1984: Clarendon Press.

[66] FLIR Systems, I. *Specifications of FLIR A325sc Infrared Cameras*. 2013; Available from: http://www.flir.com/thermography/americas/us/view/?id=46623&collectionid=516&col=45866.

[67] Portillo, J., et al., *Precession electron diffraction assisted orientation mapping in the transmission electron microscope*, 2010: Saltillo, Coahuila. p. 1-7.

[68] Gammer, C., et al., *Quantitative local profile analysis of nanomaterials by electron diffraction.* Scripta Materialia, 2010. **63**(3): p. 312-315.

[69] Abolghasem, S., et al., *Mapping subgrain sizes resulting from severe simple shear deformation.* Acta Materialia, 2012. **60**(1): p. 376-386.

[70] Umbrello, D., R. M'Saoubi, and J.C. Outeiro, *The influence of Johnson-Cook material constants on finite element simulation of machining of AISI 316L steel.* International Journal of Machine Tools and Manufacture, 2007. **47**(3-4): p. 462-470.

[71] Johnson, G.R.C., W.H., *A CONSTITUTIVE MODEL AND DATA FOR METALS SUBJECTED TO LARGE STRAINS, HIGH STRAIN RATES AND HIGH TEMPERATURES*, in *7th International Symposium on Ballistics*1983. p. 541–547.

[72] Adibi-Sedeh, A.H., V. Madhavan, and B. Bahr, *Extension of Oxley's analysis of machining to use different materials models.* Journal of Manufacturing Science and Engineering, Transactions of the ASME, 2003. **125**(4): p. 656-666.

[73] Chandrasekaran, H., R. M'Saoubi, and H. Chazal, *Modelling of material flow stress in chip formation process from orthogonal milling and split hopkinson bar tests.* Machining Science and Technology, 2005. **9**(1): p. 131-145.

[74] Kapoor, R. and S. Nemat-Nasser, *Determination of temperature rise during high strain rate deformation.* Mechanics of Materials, 1998. **27**(1): p. 1-12.

[75] Cullity, B.D. and S.R. Stock, *Elements of x-ray diffraction*. 2001: Prentice Hall.

[76] Dickson, M., *The significance of texture parameters in phase analysis by X-ray diffraction.* Journal of Applied Crystallography, 1969. **2**(4): p. 176-180.

[77] Huang, H., J. Ding, and P.G. McCormick, *Microstructural evolution of 304 stainless steel during mechanical milling.* Materials Science and Engineering: A, 1996. **216**(1–2): p. 178-184.

[78] Fultz, B. and J.M. Howe, *Transmission electron microscopy and diffractometry of materials*. 2002: Springer London, Limited.

[79] Kashyap, B.P. and K. Tangri, *On the Hall-Petch relationship and substructural evolution in type 316L stainless steel.* Acta Metallurgica Et Materialia, 1995. **43**(11): p. 3971-3981.

[80] Grewal, H.S., et al., *Surface modification of hydroturbine steel using friction stir processing.* Applied Surface Science, 2013. **268**: p. 547-555.

[81] Schino, A.D., M. Barteri, and J.M. Kenny, *Development of ultra fine grain structure by martensitic reversion in stainless steel.* Journal of Materials Science Letters, 2002. **21**(9): p. 751-753.

[82] Karimi, M., et al., *Effect of martensite to austenite reversion on the formation of nano/submicron grained AISI 301 stainless steel.* Materials Characterization, 2009. **60**(11): p. 1220-1223.

[83] Huang, J., et al., *Enhanced mechanical properties of type AISI301LN austenitic stainless steel through advanced thermo mechanical process.* Materials Science and Engineering A, 2012. **532**: p. 190-195.

[84] Black, M.P. and R.L. Higginson, *Investigation into the use of electron back scattered diffraction to measure recrystallised fraction.* Scripta Materialia, 1999. **41**(2): p. 125-129.

[85] Thompson, C.V. and R. Carel, *Stress and grain growth in thin films.* Journal of the Mechanics and Physics of Solids, 1996. **44**(5): p. 657-673.

[86] Gianola, D.S., et al., *Stress-assisted discontinuous grain growth and its effect on the deformation behavior of nanocrystalline aluminum thin films.* Acta Materialia, 2006. **54**(8): p. 2253-2263.